Article

Cell Reports

Paneth Cells Respond to Inflammation and Contribute to Tissue Regeneration by Acquiring Stem-like Features through SCF/c-Kit Signaling

Graphical Abstract

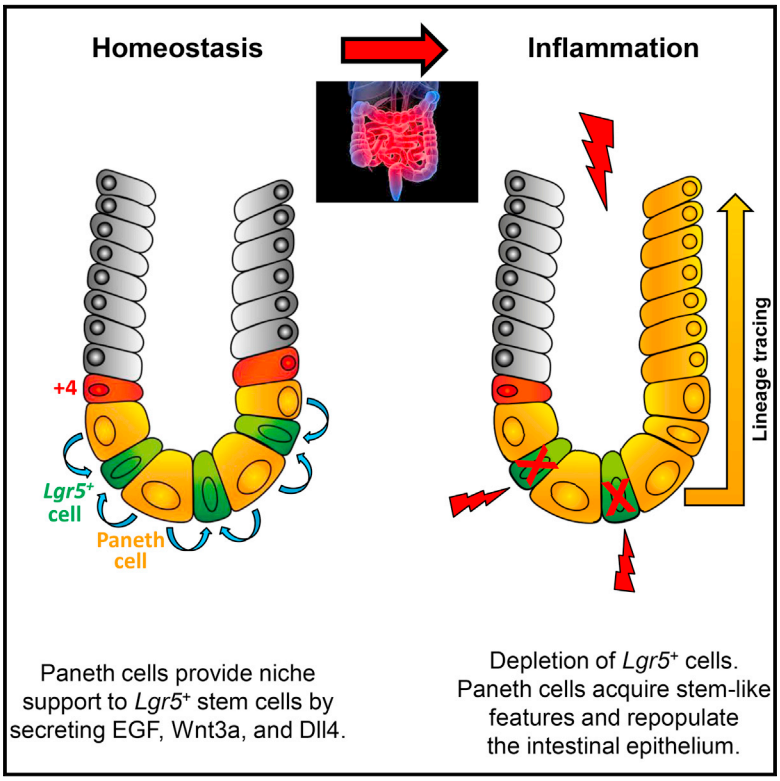

Highlights

- Inflammation of the mouse small intestine leads to loss of *Lgr5*$^{+}$ stem cells
- Inflammation results in an overall increase in intestinal stem cell function
- Paneth cells respond to inflammation by acquiring stem-like features
- Activation of the SCF/cKit/Wnt signaling axis underlies Paneth cell de-differentiation

Authors

Mark Schmitt, Matthias Schewe, Andrea Sacchetti, ..., Johan van Es, Hans Clevers, Riccardo Fodde

Correspondence

r.fodde@erasmusmc.nl

In Brief

Schmitt et al. show that inflammation of the mouse small intestine results in dramatic loss of the resident stem cells, followed by de-differentiation of highly specialized secretory units called Paneth cells. These findings are relevant for our understanding of tissue response in inflammatory bowel syndromes and their increased cancer risk.

Schmitt et al., 2018, Cell Reports *24*, 2312–2328
August 28, 2018
https://doi.org/10.1016/j.celrep.2018.07.085

CellPress

OPEN ACCESS
CellPress

Cell Reports
Article

Paneth Cells Respond to Inflammation and Contribute to Tissue Regeneration by Acquiring Stem-like Features through SCF/c-Kit Signaling

Mark Schmitt,[1,5] Matthias Schewe,[1,5] Andrea Sacchetti,[1] Danny Feijtel,[1] Wesley S. van de Geer,[2] Miriam Teeuwssen,[1] Hein F. Sleddens,[1] Rosalie Joosten,[1] Martin E. van Royen,[3] Harmen J.G. van de Werken,[2] Johan van Es,[4] Hans Clevers,[4] and Riccardo Fodde[1,6,*]

[1]Department of Pathology, University Medical Center, Rotterdam, the Netherlands
[2]Cancer Computational Biology Center and Department of Urology, University Medical Center, Rotterdam, the Netherlands
[3]Erasmus Optical Imaging Center, Erasmus MC Cancer Institute, University Medical Center, Rotterdam, the Netherlands
[4]Hubrecht Institute, University Medical Center Utrecht and Princess Maxima Center, Utrecht, the Netherlands
[5]These authors contributed equally
[6]Lead Contact
*Correspondence: r.fodde@erasmusmc.nl
https://doi.org/10.1016/j.celrep.2018.07.085

SUMMARY

IBD syndromes such as Crohn's disease and ulcerative colitis result from the inflammation of specific intestinal segments. Although many studies have reported on the regenerative response of intestinal progenitor and stem cells to tissue injury, very little is known about the response of differentiated lineages to inflammatory cues. Here, we show that acute inflammation of the mouse small intestine is followed by a dramatic loss of *Lgr5*$^+$ stem cells. Instead, Paneth cells re-enter the cell cycle, lose their secretory expression signature, and acquire stem-like properties, thus contributing to the tissue regenerative response to inflammation. Stem cell factor secretion upon inflammation triggers signaling through the c-Kit receptor and a cascade of downstream events culminating in GSK3β inhibition and Wnt activation in Paneth cells. Hence, the plasticity of the intestinal epithelium in response to inflammation goes well beyond stem and progenitor cells and extends to the fully differentiated and post-mitotic Paneth cells.

INTRODUCTION

Adult stem cells have long been postulated to be intrinsically of a slow-cycling nature, mainly based on the necessity to preserve the integrity of their genome by preventing mutations occurring during DNA replication (Fuchs, 2009). In the hematopoietic field in particular, there is general consensus regarding the inverse correlation between cycling frequency and long-term stem cell activity (Orford and Scadden, 2008). However, tissues characterized by a high cellular turnover (e.g., intestine, skin) seem to represent notable exceptions to these rules of thumb because highly proliferative stem cells—e.g., the *Lgr5*$^+$ crypt base columnar (CBC) cells in the intestinal crypt of Lieberkühn (Barker et al., 2007)—have a remarkable long-term self-renewal capacity. In these cases, a dichotomy of cycling and more quiescent stem cell lineages is thought to coexist within the niche; although actively cycling stem cells underlie daily homeostasis, their more quiescent equivalents are thought to play key roles in the response to tissue damage, upon which they re-enter the cell cycle, thus contributing to the regeneration process (Fuchs, 2009).

In the intestinal epithelium, *Lgr5*$^+$ stem cells are positioned at the very crypt bottom (position +1), usually flanked on both sides by secretory Paneth cells (PCs) in the small intestine and by analogous Paneth-like cells in the colon (Rothenberg et al., 2012; Sasaki et al., 2016; Sato et al., 2011; Schewe et al., 2016). Of note, apart from their canonical antimicrobial function, exerted through the secretion of bactericidal compounds into the lumen (Clevers and Bevins, 2013), PCs have also been shown to play an essential niche role in supporting *Lgr5*$^+$ CBC cells both through cell-cell contacts and by secreting specific factors such as epidermal growth factor (EGF), Wnt3a, and Dll4 (Sato et al., 2011).

As for the less proliferative intestinal stem cell types, to date, several candidates have been identified and partially characterized (Roth and Fodde, 2011). Among others, cells located at position +4 from the base of the crypt and earmarked by *Bmi1* expression have been shown to self-renew and give rise to all of the differentiated cell lineages of the small intestine epithelium (Sangiorgi and Capecchi, 2008). Notably, the +4 position of these *Bmi1*$^+$ stem cells is reminiscent of the bromodeoxyuridine (BrdU)-retaining cells originally identified by Potten (1998). However, the marker genes identified to date as proxies of these quiescent cell types are often not unique to a specific stem cell lineage but, rather, co-expressed at lower levels in other cells (Clevers, 2016; Grün et al., 2016; Li et al., 2014; Muñoz et al., 2012).

Previously, we employed an *in vivo* label-retaining method as a marker-free approach for the isolation of infrequently dividing cells and identified PCs and their precursors as the least cycling and longest-lasting intestinal cell lineage. Notably, we showed that, upon tissue injury, these secretory cells and their immature precursors are capable of losing expression of some

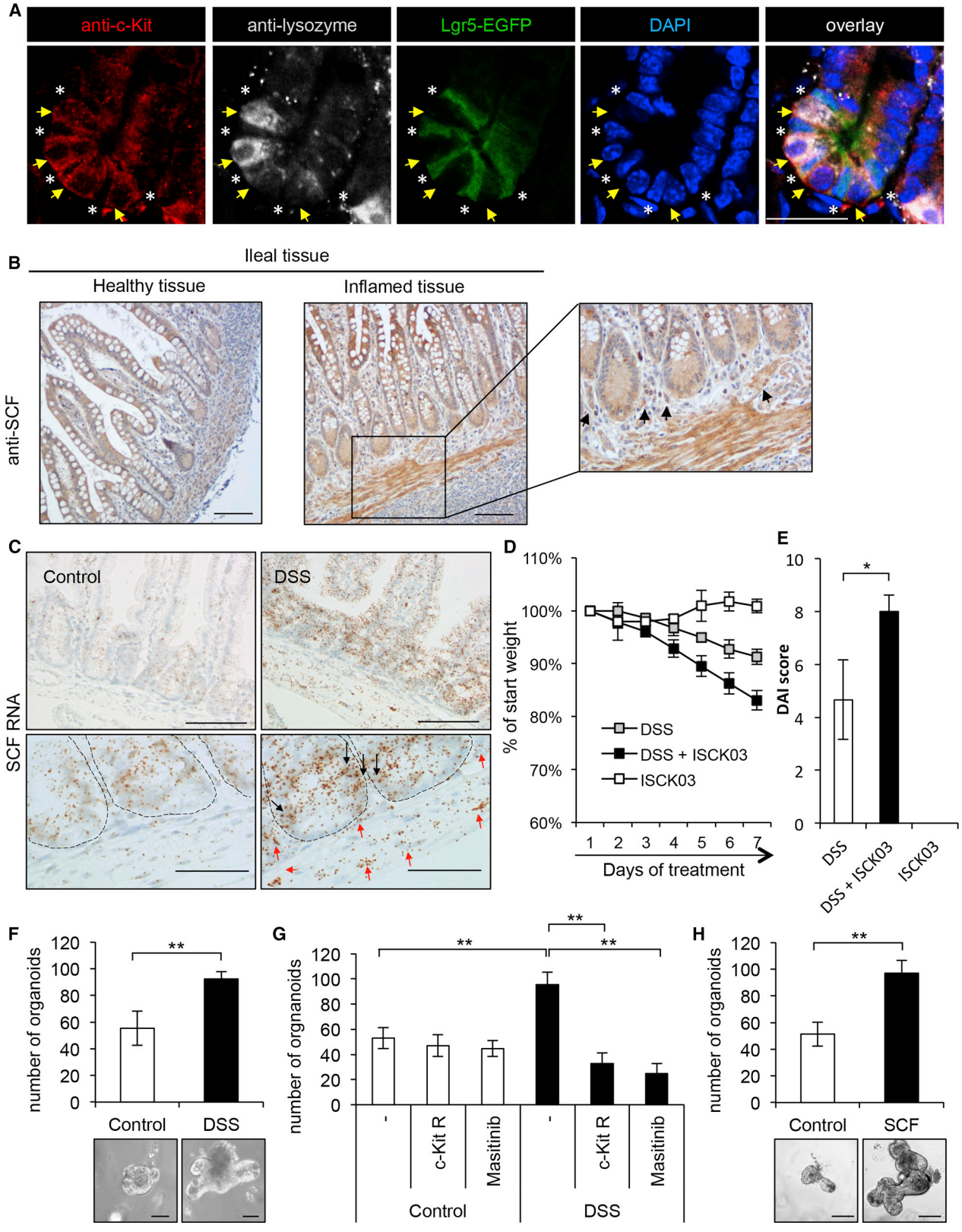

(legend on next page)

Paneth-specific genes (Roth et al., 2012). More recently, Buczacki et al. (2013) showed that label-retaining cells located at around position +3/+4 represent precursors committed to the Paneth and entero-endocrine lineages but are also potentially capable of giving rise to all intestinal cell types. These findings suggest that committed progenitors, and possibly even fully differentiated and post-mitotic intestinal lineages, as postulated in the present study, may serve as an alternative source of stem cells contributing to the regenerative response to tissue damage. Accordingly, irradiation-induced injury is usually accompanied by loss of CBC cells and de-differentiation of secretory progenitor cells earmarked by *Dll1* expression (usually located at position +5 or higher) into stem-like cells (van Es et al., 2012). In addition to secretory lineages, enterocyte progenitors expressing the intestinal alkaline phosphate (*Alpi*) gene have also been shown to regain stem cell potential upon *Lgr5*$^{+}$ CBCs ablation (Tetteh et al., 2016).

The role played by precursors of secretory lineages, and in particular by PCs, in the regenerative response to intestinal tissue damage is of interest especially in the context of inflammatory bowel disease (IBD), a cumulative name for syndromes such as Crohn's disease (CD) and ulcerative colitis (UC) featuring chronic inflammation of either both the small and large intestine (CD) or only the colon (UC) (Clevers and Bevins, 2013; Schewe and Fodde, 2018). In particular, CD has been shown to be a disorder of the PC, and, vice versa, PCs are regarded as the site of origin of intestinal inflammation in CD because defects in its unfolded protein response function are likely to trigger the inflammatory reaction (Adolph et al., 2013).

In this study, we elucidated the role played by PCs, a terminally differentiated and post-mitotic secretory lineage, in the regenerative response to inflammation and its capacity to de-differentiate and acquire stem cell characteristics to contribute to intestinal regeneration. Of note, the expression of stem cell factor (SCF) (i.e., the ligand of the c-Kit receptor specifically expressed in PCs) is enhanced in IBD patients, and the DSS (dextran sodium sulfate) model. Indeed, the mechanisms underlying PC de-differentiation and stemness acquisition rely on activation of phosphatidylinositol 3-kinase (PI3K)/Akt and Wnt downstream of the SCF/c-Kit signaling axis.

RESULTS

Intestinal Expression of the c-Kit Ligand SCF Is Enhanced in IBD Patients and in Mouse Models of Pan-gastroenteritis

It has been reported previously that the expression of SCF is increased in IBD patients (Andersson et al., 2017; Comar et al., 2012). This observation is of potential interest because the *SCF* gene, also known as *KITLG*, encodes the ligand of the tyrosine-kinase receptor c-KIT, known to regulate the survival, maintenance, and self-renewal of stem cells (Lennartsson and Rönnstrand, 2012). Of note, both secretory PCs in the small intestinal epithelium (Figure 1A, arrows) and Paneth-like cells (PLCs) in the colon express the c-KIT receptor (Rothenberg et al., 2012). In contrast, *Lgr5*$^{+}$ CBC cells do not express c-KIT (Figure 1A, asterisks; Clevers, 2016; Grün et al., 2016; Li et al., 2014; Muñoz et al., 2012). In view of the known niche role played by PCs in supporting *Lgr5*$^{+}$ stem cells (Sato et al., 2011) their own capacity to respond to tissue damage by re-entering the cell cycle and acquiring stem-like cell properties (Buczacki et al., 2013; Roth et al., 2012; Schewe et al., 2016), we set out to study the functional significance of SCF activation upon inflammatory insults by first validating the upregulation of SCF expression in IBD patients (i.e., CD and UC) and in the DSS mouse model of acute intestinal inflammation of the entire GI tract (pan-gastroenteritis) (Elsheikh et al., 2012).

SCF immunohistochemistry (IHC) analysis of a small cohort of IBD patients (n = 9, of which 5 had UC and 4 had CD, together with normal tissues from two colorectal cancer patients as controls) revealed increased expression in the epithelial lining and the mucosa and submucosa of the inflamed small intestinal and colon tissues from CD and UC patients, respectively (Figures 1B and S1A). As expected, PC metaplasia was also frequently observed in the colon of the analyzed IBD patients (3 of 5 UC patients; Figure S1B). Next we analyzed SCF expression in the DSS mouse model. DSS was administered orally (3% in drinking water) for a week to cause acute inflammation. On day 7 of DSS treatment, intestinal tissues were harvested and analyzed for SCF expression by RNA *in situ* hybridization, which confirmed increased SCF expression in the small intestinal

Figure 1. SCF Expression Is Increased upon Intestinal Inflammation and Positively Affects Organoid Growth

(A) Confocal microscopy analysis of *Lgr5*$^{EGFP\text{-}IRES\text{-}creERT2}$ mice using antibodies against lysozyme and c-Kit. c-Kit is detected at the membrane of Lyz^{+} PCs (arrows) but not on GFP-labeled Lgr5^{+} cells (asterisks) (scale bar, 25 μm).

(B) Comparison by IHC analysis of SCF expression in healthy (left) and CD-derived small intestinal tissues (right). The arrowheads indicate SCF-expressing cells close to the intestinal crypts. The images are representative of 2 healthy and 4 CD patients; scale bars, 100 μm.

(C) SCF *in situ* hybridization (ISH) analysis of small intestinal tissues derived from control (top) and DSS-treated (bottom) mice 1 day after DSS removal. Increased SCF RNA levels can be observed in the intestinal epithelium and submucosa of inflamed mice. Pictures show representative examples of n = 3 mice; scale bars, 200 μm (top) and 50 μm (bottom); grid lines indicate intestinal crypts. Red (stromal) and black (intestinal epithelial) arrows indicate cells with increased SCF expression in proximity to PCs.

(D) Weight loss graphs relative to mice treated with 3% DSS alone, ISCK03 alone (0.1 mg/mL in the drinking water), and 3% DSS + ISCK03 for 7 days (n = 6 for DSS and DSS + ISCK03-treated mice; n = 3 for ISCK03-treated mice).

(E) DAI score relative to the mice described in (B) (*$p < 0.05$); mean (SD) values are shown. Details of scoring are shown in Figure S1D and STAR Methods.

(F) Organoid multiplicities from whole crypts of control and 3% DSS-treated mice (7 days). Crypts were isolated and plated 3 days after DSS withdrawal. Pictures show representative organoids of each condition on day 5 of culture (scale bars, 50 μm; **$p < 0.01$; n = 4; mean [SD] values are shown).

(G) Organoid multiplicities from whole crypts of control and 3% DSS-treated mice (7 days). Crypts were plated 3 days after DSS withdrawal in the presence or absence of the soluble c-Kit receptor (500 ng/mL) or masitinib (200 nM) (**$p < 0.01$, n = 3; mean [SD] values are shown).

(H) Organoid multiplicities from whole crypts grown in control medium with or without murine SCF (50 ng/mL). Pictures show representative organoids of each condition on day 5 of culture (scale bars, 50 μm; **$p < 0.01$; n = 3; mean [SD] values are shown).

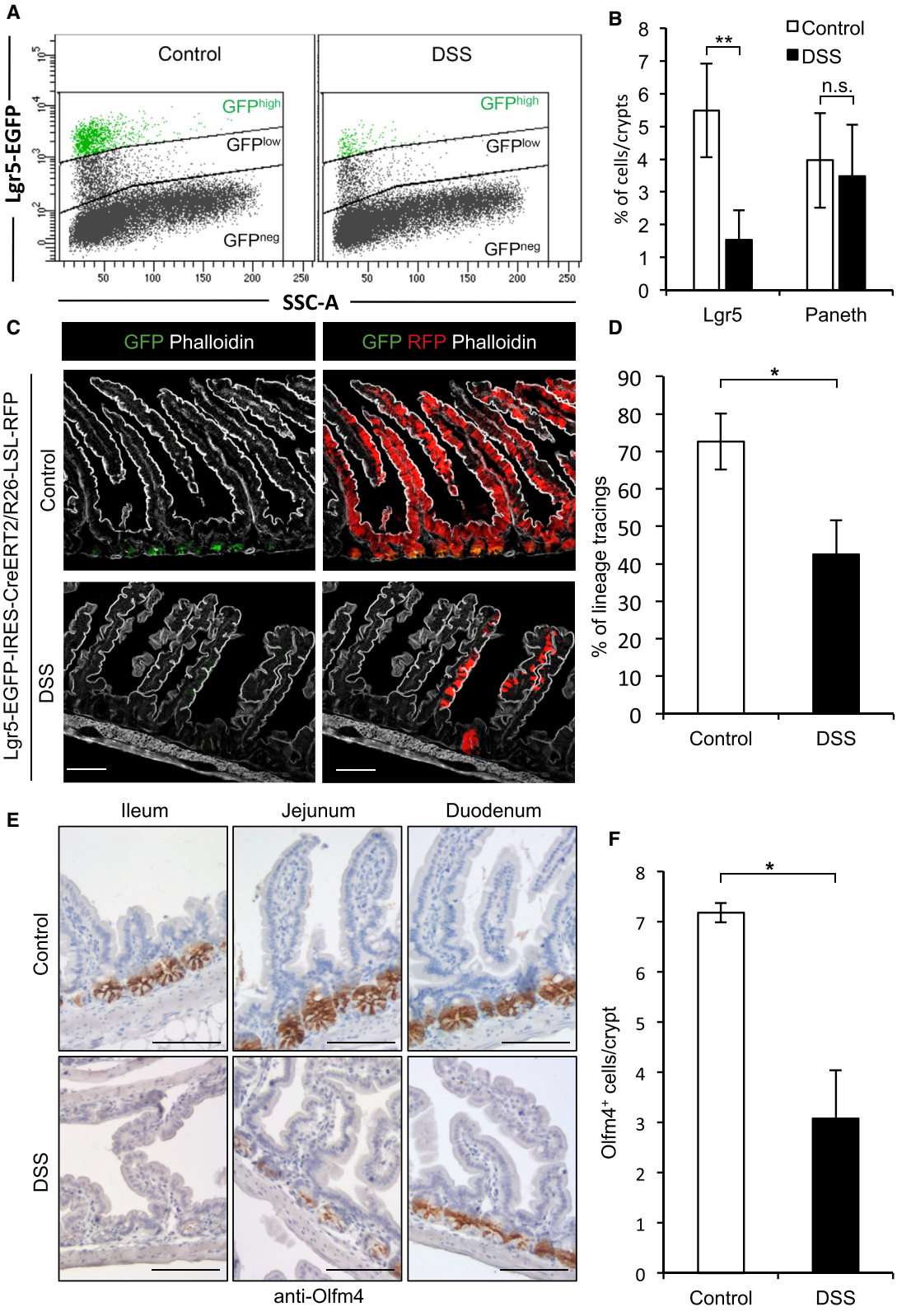

(legend on next page)

epithelium as well as the mucosa and submucosa of the treated mice (Figures 1C and S1C). RNA probes against PPIB (peptidylprolyl *cis-trans* isomerase B), here employed as positive controls, showed no differences between control and DSS-treated mice (Figure S1C).

To assess whether increased SCF/c-Kit signaling plays a critical role during intestinal inflammation, we inhibited the pathway by administrating the specific c-Kit inhibitor ISCK03 in the drinking water together with DSS (Na et al., 2007). ISCK03 alone had no effect on the overall health of the animals, as shown by their unchanged body weight (Figure 1D), disease activity index (DAI; Figures 1E and S1D), and infiltrating $CD3^+$ T lymphocyte multiplicity (Figures S1E and S1F) compared with control mice. However, mice treated with ISCK03 in combination with DSS suffered more severely compared with mice treated with DSS alone, as shown by increased weight loss and DAI scores (Figures 1D and 1E and S1D) and number of infiltrating $CD3^+$ T lymphocytes (Figure S1E).

Overall, these results confirm that expression of the c-Kit ligand SCF is enhanced upon intestinal inflammation and that activation of the SCF/c-Kit signaling axis is critical in the physiological response to the inflammatory insult. In view of the multifunctional nature of PCs and their expression of the c-Kit receptor, we set out to analyze the functional consequences of the activation of the SCF/c-Kit signaling axis on the intestinal stem cell niche.

Inflammation-Driven SCF Expression Enhances Intestinal Stem Cell Function

To study the effects of inflammation and enhanced SCF expression on the intestinal stem cell niche, we employed *ex vivo* "mini-gut" organoid formation as a readout of stemness (Sato et al., 2009; Schewe et al., 2016). To this aim, we administered 3% DSS in the drinking water to C57BL/6J mice for 1 week and collected small intestinal crypts to assess their ability to form organoids on day 3 after withdrawal of DSS; i.e., at the peak of the regenerative response. As shown in Figure 1F, DSS treatment resulted in a significant increment in organoid multiplicity (~2-fold). Moreover, organoids from DSS-treated mice were of increased size and more complex morphology (increased number of budding events) compared with the organoids from control animals (Figure 1F).

To assess the role of increased SCF expression on the observed positive effect of DSS-driven inflammation on intestinal stem cell function, we harvested crypts from DSS-treated and control mice and supplemented the culture medium with a soluble c-Kit receptor able to bind and sequester SCF, preventing its interaction with its membrane-bound receptor (Dahlen et al., 2001). In parallel, c-Kit activity was also repressed by using the receptor tyrosine kinase inhibitor masitinib (Dubreuil et al., 2009). Although both the c-Kit receptor and masitinib had no significant effect on organoids derived from control animals, they substantially abrogated the increased organoid multiplicity observed in DSS-treated mice (Figure 1G).

Next we tested whether SCF alone was sufficient to improve organoid formation. As depicted in Figure 1H, the presence of SCF in the culture medium increased the overall number of intestinal organoids as well as the complexity of their morphology to a very similar degree as that observed in organoids of from DSS-treated animals (~2-fold).

Hence, enhanced SCF expression upon inflammation appears to play a critical role in the tissue's regenerative response by improving intestinal stem cell function.

$Lgr5^+$ Stem Cells Are Depleted upon Inflammation

The observed positive effect of SCF on intestinal stem cell function in the regenerative response to inflammation raises the question of whether this is mediated by an increase in self-renewal and overall multiplicity of $Lgr5^+$ stem cells. To this aim, we administered 3% DSS to $Lgr5^{EGFP}$ (*Lgr5–EGFP*–internal ribosome entry site (*IRES*)–*CreERT2*) (Barker et al., 2007) reporter mice for 7 days, followed by a 3-day recovery phase, to then determine $Lgr5^+$ and PC multiplicity by fluorescence-activated cell sorting (FACS). Notably, $Lgr5^+$ cell multiplicity was severely decreased in DSS-treated animals (~3 fold; Figures 2A, 2B, S2A, and S2B), indicative of severe loss of intestinal stem cells upon acute inflammation. No significant change in PC multiplicity was observed upon DSS treatment compared with control mice (Figures 2B and S2A).

We then compared the lineage tracing ability of $Lgr5^+$ stem cells between control and DSS-treated mice. To this aim, we treated *Lgr5*-EGFP-IRES-CreERT2/R26-lox-stop-lox (LSL)-red fluorescent protein (RFP) mice with tamoxifen to trigger recombination and lineage tracing from $Lgr5^+$ CBC cells. These animals were administered 3% DSS for 1 week to then be analyzed on day 3 after withdrawal of DSS. In line with the FACS data, confocal microscopy revealed severe loss of $Lgr5^+$ CBC cells and a severe reduction of *Lgr5*-derived lineage tracing in the small intestine of DSS-treated mice (Figures 2C, 2D, and S2B). Of note, the residual tracing events extend throughout the length of the crypt villus axis, suggesting that $Lgr5^+$ stem cells that escape DSS treatment fully retain their self-renewal and differentiation capacity.

Figure 2. DSS-Induced Intestinal Inflammation Causes Loss of Intestinal Stem Cells

(A) FACS analysis of $Lgr5^+$ cells from control or DSS-treated mice 3 days after DSS withdrawal (FACS plots are representatives of 5 independent experiments; *Lgr5*-$EGFP^{high}$ cells are labeled in green).

(B) Average percentage of $Lgr5^+$ and PCs in control and DSS-treated mice, as quantified by FACS (**$p < 0.01$; n.s., not significant; n = 5; mean [SD] values are shown).

(C) Confocal microscopy images of small intestinal tissues from tamoxifen-treated $Lgr5^{EGFP\text{-}IRES\text{-}creERT2}/R26^{LSL\text{-}RFP}$ mice kept on normal or 3% DSS-supplemented drinking water for 7 days. Tissues were harvested 3 days after withdrawal of DSS.

(D) Quantification of lineage tracings events in control and DSS-treated $Lgr5^{EGFP\text{-}IRES\text{-}creERT2}/R26^{LSL\text{-}RFP}$ mice (n = 3, *$p < 0.05$; mean [SD] values are shown).

(E) Olfm4 IHC analysis of intestinal tissues from control and DSS-treated mice 1 day after removal of DSS.

(F) Quantification of $Olfm4^+$ cells/crypt from control and DSS-treated mice (n = 4, *$p < 0.05$; mean [SD] values are shown).

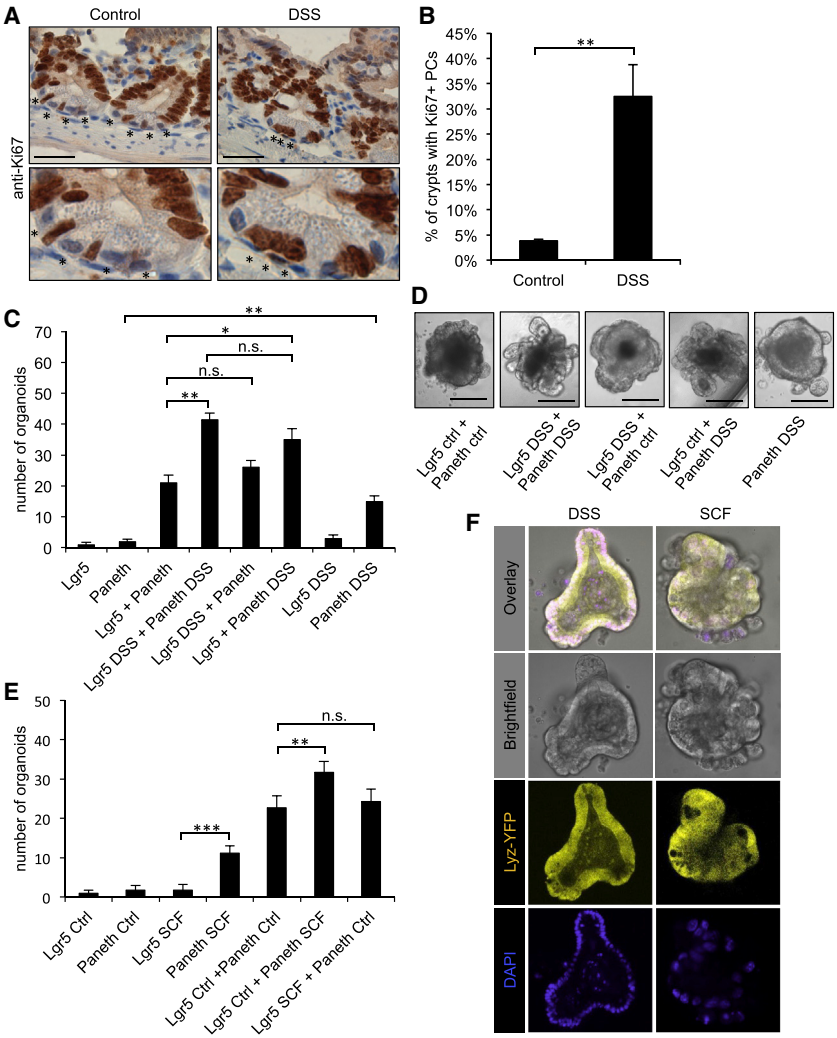

Figure 3. Inflammation Induces Proliferation and De Novo Organoid Formation from PCs via Activation of the SCF/c-Kit Signaling Axis

(A) Ki67 IHC analysis of mouse small intestinal tissues from control and DSS-treated mice 1 day after DSS removal. Asterisks indicate Ki67-negative PCs in control mice (left) and Ki67$^+$ PCs in DSS-treated mice (right) (scale bars, 25 μm (top); bottom, enlarged).

(B) Average percentage of Ki67$^+$ PCs in control and DSS-treated mice (**$p < 0.01$, $n = 4$; mean [SD] values are shown).

(C) Organoid reconstitution assay of *Lgr5*$^+$ and PCs from control and DSS-treated mice (*$p < 0.05$, **$p < 0.01$, $n = 3$; mean [SD] values are shown).

(D) Pictures showing representative examples of organoids derived from the reconstitution assays in (C) on day 7 of culture (scale bars, 100 μm).

(E) Organoid reconstitution assay of untreated and SCF-treated (50 ng/mL) *Lgr5*$^+$ and PCs (**$p < 0.01$, ***$p < 0.005$, $n = 3$; mean [SD] values are shown).

(F) Left: organoids derived from PCs of tamoxifen-injected and DSS-treated *Lys*^{CreERT2}/*R26*$^{LSL\text{-}YFP}$ mice. Right: organoids derived from SCF-treated PCs of tamoxifen-injected *Lys*^{CreERT2}/*R26*$^{LSL\text{-}YFP}$ mice.

To rule out that DSS-driven inflammation suppresses *Lgr5* gene expression without affecting intestinal CBC cells, we performed IHC analysis on intestinal tissues from DSS-treated mice with an antibody directed against the Olfm4 protein, whose expression overlaps with that of *Lgr5* (van der Flier et al., 2009a). As shown in Figures 2E, 2F, and S2C, a significant reduction in Olfm4$^+$ cells is evident in intestinal crypts from DSS-treated animals, especially at the crypt base, where they normally are intermingled with PCs.

Altogether, these results demonstrate that acute inflammation causes severe loss of intestinal stem cells, which are consequently no longer capable of contributing to the regenerative response to tissue damage.

PCs Underlie Enhanced Intestinal Stem Cell Function upon Inflammation

The loss of *Lgr5*$^+$ stem cells upon acute inflammation is in sharp contrast with the positive effect exerted by DSS on intestinal stem cell function, as shown by organoid assays. To assess whether any de novo proliferating cell type is detectable in the intestinal crypt upon inflammation, we performed Ki67 staining on small intestinal tissue from DSS-treated and control mice. In the latter, Ki67 expression is restricted to the slender CBC cells (*Lgr5*$^+$) cells at the bottom of the crypt and the transient amplifying compartment, whereas the post-mitotic PCs are negative (Figure 3A, left). In DSS-treated mice however, apart from the absence of cells morphologically similar to CBC cells, the granulated PCs are Ki67-positive (Figure 3A, right). We confirmed the PC identity of these Ki67$^+$ cells by confocal microscopy; lysozyme/Ki67 double-positive cells are present in the intestinal crypts of DSS-treated mice (Figure S3A). Quantification of the number of crypts encompassing Ki67$^+$ PCs (>30%) highlights the relatively high frequency of reacquisition of proliferative capacity by PCs upon tissue damage (Figure 3B). Notably, Ki67$^+$ PCs could also be detected in the inflamed ileal tissues of CD patients (Figure S3B; 2 of 4).

In view of these and previous results (Roth et al., 2012), we addressed the functional role played by these secretory cells in the regenerative response of the intestinal stem cell niche to the inflammatory insult. To this aim, the organoid reconstitution assay (ORA) was employed (Sato et al., 2011; Schewe et al., 2016, 2017; Yilmaz et al., 2012). Here, *Lgr5*$^+$ and PCs are sorted by FACS from control and DSS-treated *Lgr5*^{EGFP} mice (3 days after DSS treatment; i.e., when de novo *Lgr5*$^+$ cells are not yet observed) to then be reconstituted in different combinations to form intestinal organoids (Figures 3C and 3D). As expected, reconstitution of *Lgr5*$^+$ with PCs from control mice led to the formation of organoids, whereas neither *Lgr5*$^+$ nor PCs alone were able to form organoids. Reconstitution of *Lgr5*$^+$ and PCs from

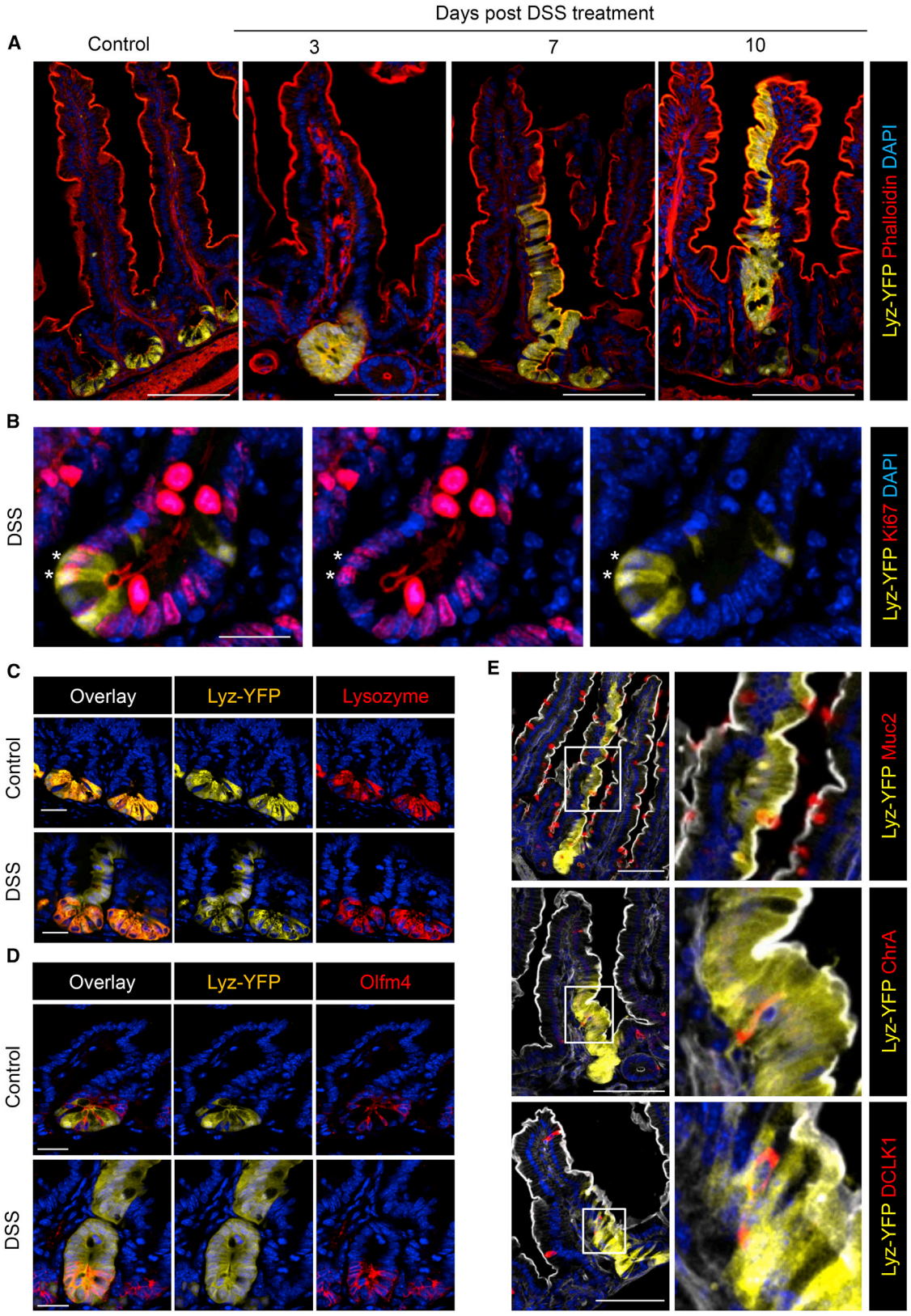

(legend on next page)

DSS-treated mice resulted in a significant increase in organoid numbers, similar to the effect of DSS on organoid formation from whole intestinal crypts. Reconstitution of *Lgr5*$^{+}$ cells from DSS-treated mice with PCs from controls did not differ in organoids numbers from the control (both cell types from untreated mice), suggesting that the stem cell function of the residual *Lgr5*$^{+}$ cells, as also observed *in vivo* (Figure 2C), is unaffected. Last, PCs from DSS-treated mice reconstituted with control *Lgr5*$^{+}$ stem cells resulted in a significant increase in organoid multiplicity compared with the reconstitution of control *Lgr5*$^{+}$ and PCs. Of note, the number of organoids generated when control *Lgr5*$^{+}$ cells were reconstituted with PCs from DSS-treated mice was very similar to the organoid multiplicity observed when both lineages were obtained from DSS-treated mice ($p = 0.15$). This indicates that the enhanced stem cell function elicited by inflammation is influenced by PCs, possibly through their previously reported niche role in support of *Lgr5*$^{+}$ stem cells (Sato et al., 2011). However, the observed proliferative response of PCs to inflammation suggests alternative scenarios where the post-mitotic secretory cells directly contribute to tissue regeneration by de-differentiation and acquisition of stem cell features. Indeed, PCs from DSS-treated mice were able to form organoids autonomously (i.e., in the absence of *Lgr5*$^{+}$ cells) (Figures 3C and 3D).

Next we took advantage of the ORA by exposing Paneth (and *Lgr5*$^{+}$) cells sorted from control mice to recombinant SCF prior to their reconstitution in different combinations (Figure 3E). As expected, untreated *Lgr5*$^{+}$ cells or PCs gave rise to very low numbers of organoids when plated alone. The latter was also true for *Lgr5*$^{+}$ cells pretreated with *SCF*. However, SCF treatment of PCs resulted in a striking increase in organoid multiplicity (approximately 10-fold). Accordingly, reconstitution of SCF-treated *Lgr5*$^{+}$ cells with untreated PCs did not affect the number of organoids compared with the controls. Instead, SCF-treated PCs gave rise to the highest organoid multiplicity when reconstituted with untreated *Lgr5*$^{+}$ cells (Figure 3E).

To provide definitive evidence of the PC origin of these organoids, we repeated the DSS treatments and organoid experiments using *Lys*^{CreERT2}/*R26*$^{LSL\text{-}YFP}$ mice and YFP^{+} PCs isolated during the regenerative phase. The resulting organoids were entirely composed of YFP^{+} cells, confirming that, upon inflammation, PCs acquire stem cell features and give rise to mini-gut structures *ex vivo* (Figure 3F, left). Also in the case of SCF treatment, we repeated the experiment with PCs from tamoxifen-treated *Lys*^{CreERT2}/*R26*$^{LSL\text{-}YFP}$ mice and confirmed that the organoids are entirely composed of YFP^{+} cells (Figure 3F, right).

To demonstrate that PCs can also act *in vivo* as stem cells in response to inflammation, we administered DSS to *Lys*^{CreERT2}/*R26*$^{LSL\text{-}YFP}$ mice and analyzed their small intestine for lineage tracing events at several time points after withdrawal of DSS. In tamoxifen-treated control mice, yellow fluorescent protein (YFP) fluorescence was entirely restricted to PCs located at the crypt base (Figures 4A and 4C). However, FACS analysis of tamoxifen-treated *Lys*^{CreERT2}/*R26*$^{LSL\text{-}YFP}$ mice revealed that only a small proportion (~12%) of PCs express YFP after 3 consecutive injections of tamoxifen (2 mg/20 g body weight/day) (Figures S4A, top, and S4B). Nonetheless, virtually all (97%) of the YFP^{+} cells were confirmed to be PCs by FACS (Figures S4B, bottom, and S4D). All YFP^{+} cells were positive for c-Kit and lysozyme (Figure S4C). No YFP signal was detected prior to tamoxifen administration (Figure S4D). In DSS-treated (and tamoxifen-treated) animals, the YFP signal was still restricted to PCs at the crypt base 1 day after DSS removal (Figure S4E). However, already at this time point, a proportion of the YFP^{+} cells started to show nuclear Ki67, indicative of cell cycle re-activation in PCs (Figure 4B). Three days after DSS removal, short ribbons of YFP^{+} cells were observed within the intestinal crypts. Seven days after removal of DSS, YFP stained approximately 50%–70% of the crypt-villus axis and reached the tip of the villi on day 10 (Figure 4A). These *in vivo* results demonstrate that, upon DSS-driven acute inflammation, PCs acquire stem cell features and repopulate the intestinal epithelium, contributing to the tissue-regenerative response.

To assess the multipotency of the Paneth-derived stem cells, we carried out immunofluorescence (IF) analysis with lineage-specific markers of the YFP^{+} ribbons from DSS-treated *Lys*^{CreERT2}/*R26*$^{LSL\text{-}YFP}$ mice on day 7 of the recovery phase. As shown in Figure 4D, YFP^{+} cells located at the bottom of the crypt co-expressed Olfm4, indicating that new CBC cells are generated from lysozyme-expressing PCs. As for the YFP^{+} cells located above the crypt base and along the villus axis, expression of entero-endocrine (chromogranin A^{+} [ChrA^{+}]/YFP^{+}), goblet (Muc2^{+}/YFP^{+}), and tuft (Dclk1^{+}/YFP^{+}) lineage-specific markers was detected (Figure 4E). Hence, the Paneth-derived stem cells give rise to ribbons that recapitulate both the crypt-villus architecture and heterogeneous cell lineage composition of the intestinal epithelium.

Taken together, our results show that, upon acute inflammation PCs de-differentiate into proliferating stem-like cells able to form 3D organoids *ex vivo* and to repopulate *in vivo* the epithelial lining, giving rise to stem cells as well as all of the differentiated lineages of the adult intestinal epithelium. Activation of the SCF/c-Kit signaling pathway plays a central role in acquisition of stem-like features by PCs upon inflammation.

Activation of the SCF/c-Kit Signaling Axis and of the Downstream PI3K/Akt and Wnt Pathways Elicits Stemness in PCs upon Inflammation

SCF/c-Kit signaling has been shown to activate several downstream signaling pathways (Lennartsson and Rönnstrand,

Figure 4. PCs De-differentiate into Stem-like Cells in Response to DSS-Induced Inflammation

(A) Lineage tracing analysis of tamoxifen-injected *Lys*^{CreERT2}/*R26*$^{LSL\text{-}YFP}$ mice at several time points after DSS treatment (scale bars, 100 μm).

(B) Ki67 expression analysis of *Lys*^{CreERT2}/*R26*$^{LSL\text{-}YFP}$ mice 1 day after DSS withdrawal (scale bar, 25 μm).

(C) Analysis of lysozyme expression in *Lys*^{CreERT2}/*R26*$^{LSL\text{-}YFP}$ mice 7 days after DSS withdrawal (scale bars, 25 μm).

(D) Analysis of Olfm4 expression in *Lys*^{CreERT2}/*R26*$^{LSL\text{-}YFP}$ mice 7 days after DSS withdrawal (scale bars, 25 μm).

(E) Analysis of expression of differentiation markers (goblet cells, Muc2; entero-endocrine cells, ChrA; tuft cells, DCLK1) in *Lys*^{CreERT2}/*R26*$^{LSL\text{-}YFP}$ mice 7 days after DSS withdrawal (scale bars, 100 μm).

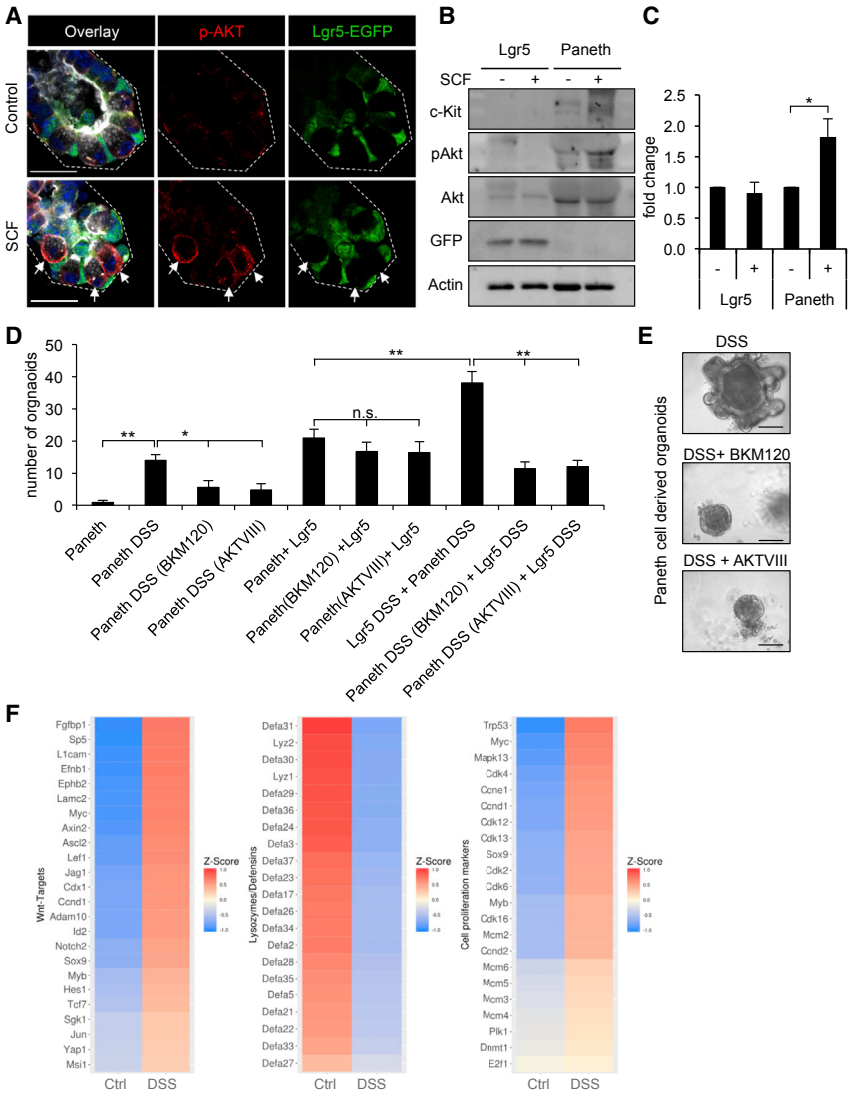

Figure 5. SCF Triggers PC De-differentiation via the PI3K/AKT Signaling Axis

(A) IF analysis of pAkt in untreated and SCF-treated (50 ng/mL) intestinal crypts from *Lgr5*-EGFP mice (arrows indicate pAkt$^+$ PCs; scale bar, 25 μm). Intestinal crypts were counterstained with DAPI and phalloidin. The picture shows one representative example from at least 3 independent experiments.

(B) Western blot analysis of untreated and SCF-treated (50 ng/mL) *Lgr5*$^+$ and PCs using antibodies against c-Kit, pAkt, total Akt, GFP, and actin.

(C) Quantification of pAkt/Akt signal intensity from the western blot in (B) (*$p < 0.05$, n = 3; mean [SD] values are shown).

(D) Organoid reconstitution assay of *Lgr5*$^+$ and PCs from control and DSS-treated mice. PCs were either left untreated or treated with BKM120 (PI3K inhibitor, 1 μM) or AKTVIII (Akt inhibitor, 4 μM) (*$p < 0.05$, **$p < 0.01$, n = 3; mean [SD] values are shown).

(E) Representative pictures of PC-derived organoids as described in (D) (scale bars, 50 μm).

(F) RNA-seq analysis of PCs from control (n = 3) and DSS-treated (n = 4) mice 3 days after DSS withdrawal. Heatmaps show differentially expressed genes (left, Wnt target genes; center, lysozymes and alpha-defensins; right, cell proliferation marker genes). Color codes indicate average *Z* scores of each condition.

2012). To assess which of these pathways may play a role in the observed de-differentiation and acquisition of stem-like features in PCs upon inflammation and the consequent SCF/c-Kit signaling activation, we treated whole small intestinal crypts with SCF in combination with several inhibitors of known downstream pathways, such as mitogen-activated protein kinase (MAPK), mechanistic target of rapamycin (mTor), PI3K/Akt and Jak/Stat signaling, and tested their capacity to form organoids (Figure S5A). As shown before, SCF treatment alone significantly increased organoid multiplicity compared with untreated crypts. MAPK signaling inhibition completely repressed organoid growth both in the presence or absence of SCF, indicating an essential role for this pathway in organoid growth independent of the activation of the SCF/c-Kit signaling axis. In contrast, the mTOR inhibitor rapamycin did not affect organoid multiplicity with or without SCF. Inhibition of Jak1 instead increased organoid numbers to the same extent both in the absence and presence of SCF. Of the 4 main downstream pathways tested, only the inhibition of PI3K/Akt signaling completely and specifically abrogated the positive effects exerted by SCF on organoid growth (Figure S5A).

To establish whether SCF activates PI3K/Akt signaling in PCs, whole intestinal crypts from *Lgr5*^{EGFP} mice were treated with SCF and analyzed by IF with antibodies directed against pan- and phosphorylated Akt (pAkt). Although Akt was expressed in all cell types of the intestinal crypt (Figure S5B), Akt phosphorylation was exclusively observed in PCs upon SCF stimulation (Figures 5A and S5C). Western blot analysis of PCs sorted by FACS and incubated with SCF confirmed the increased pAkt levels in the secretory cells. In contrast, analysis of the c-Kit negative *Lgr5*$^+$ stem cells did not reveal any change (Figures 5B and 5C).

To assess the relevance of the role played by PI3K/Akt signaling in the response to inflammation, PCs were sorted from DSS-treated mice and cultured to generate organoids in the presence of specific PI3K (BKM120; Wen et al., 2012) and Akt (AKTVIII; Barnett et al., 2005) inhibitors. In confirmation of the above result with whole intestinal crypts, both PI3K as well as Akt inhibition significantly reduced the number of organoids obtained from PCs alone (Figures 5D and 5E). Likewise, in reconstitution assays, inhibition of PI3K or Akt in PCs significantly repressed organoid growth when *Lgr5*$^+$ and PCs from DSS-treated mice were employed, although not ones from untreated mice (Figure 5D).

To evaluate the global effects of acute inflammation on PCs, we performed RNA expression analysis by next-generation

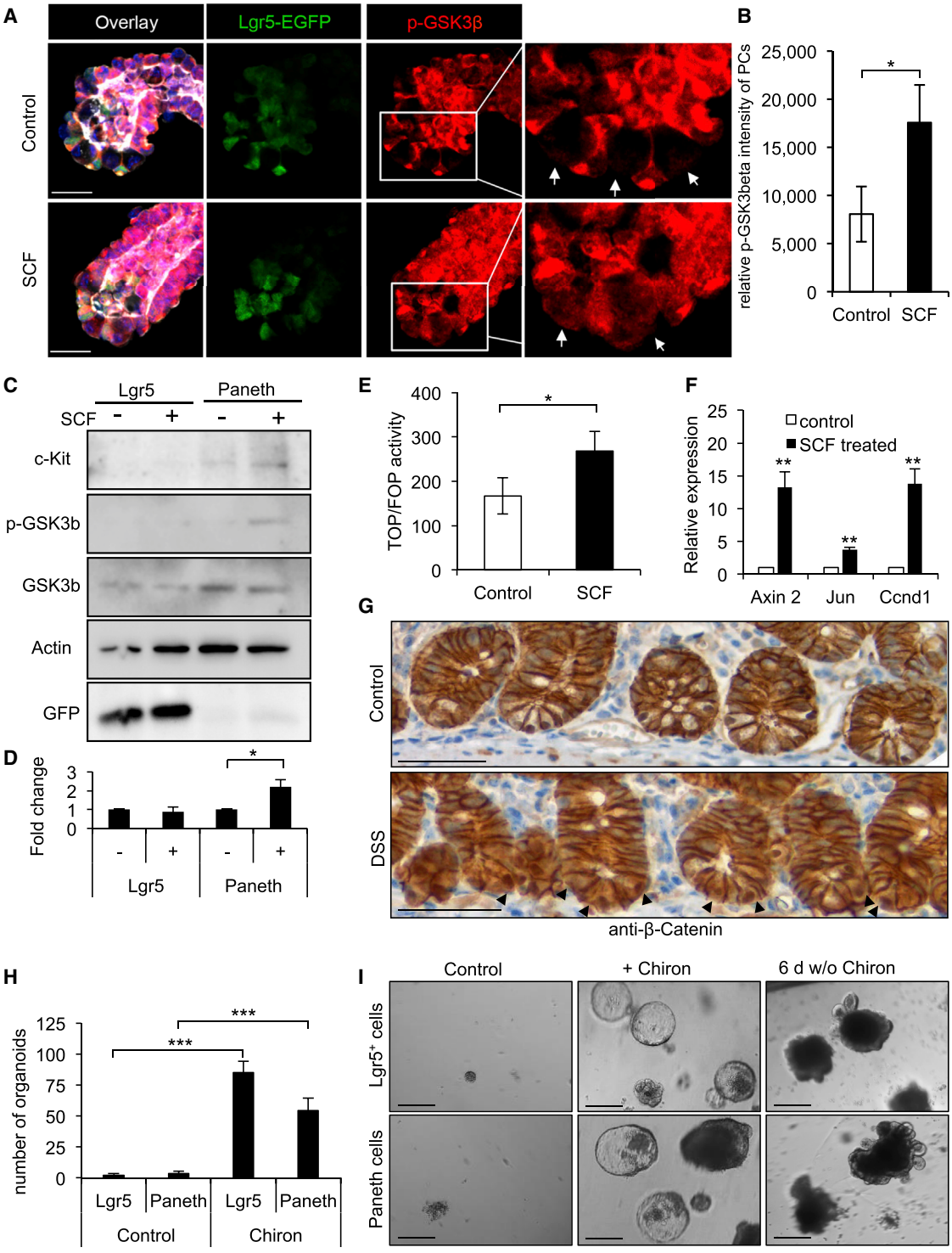

Figure 6. Activation of the SCF/c-Kit Signaling Axis Inhibits Gsk3β and Activates Wnt in PCs

(A) IF analysis of phospho-GSK3β in untreated and SCF-treated intestinal crypts from *Lgr5*-EGFP mice. Arrows indicate phospho-GSK3β-negative PCs in untreated crypts (top). Among SCF-treated crypts (bottom), phospho-GSK3β PCs become evident (also indicated by arrows; scale bars, 25 μm). Intestinal crypts were counterstained with DAPI and phalloidin. The picture shows one representative example of at least 3 independent experiments.

(B) Relative fluorescence intensity of phospho-GSK3β in PCs treated as described in (B). PCs were set as ROI (region of interest) for the measurement of phospho-GSK3β intensity (*$p < 0.05$, $n = 3$; mean [SD] values are shown).

(legend continued on next page)

sequencing (NGS) RNA sequencing (RNA-seq) on sorted cells from control and DSS-treated mice. In agreement with the *in vivo* data, the RNA-seq results revealed upregulation of genes related to cell proliferation and the cell cycle and downregulation of PC-specific markers such as lysozymes and defensins (Figure 5F). Of note, a group of genes known to earmark infrequently dividing and quiescent stem cells (i.e., *Tert*, *Ascl2*, *EphB2*, *Dclk1*, and *Lrig1*; Figure S5D) were upregulated in PCs from DSS-treated mice, whereas the expression of other stem cell markers, such as *Lgr5*, *Bmi1*, and *Hopx*, appeared to be reduced (Figure S5D).

Last, pathway analysis performed on the differentially expressed genes pointed to activation of the canonical Wnt signaling pathway, as shown by the upregulation of several Wnt target genes (Figure 5F). This is likely to be related to the observed role played by PI3K/Akt signaling downstream of SCF/cKit; it has been shown that PI3K/Akt activation can increase Wnt signaling activity through GSK3β inhibitory phosphorylation at Ser-9 (Doble and Woodgett, 2003). IF analysis of whole-mount intestinal crypts revealed that, as for Akt, GSK3β is expressed in all epithelial cells (Figure S6A). In these control crypts, *Lgr5*$^+$ stem cells as well as the proliferative transient amplifying (TA) compartment express high levels of phosphorylated GSK3β as a result of Wnt signaling activation in these lineages (Figure 6A). In contrast, PCs appear to be negative for pGSK3β, notwithstanding their characteristic nuclear β-catenin localization (van Es et al., 2005). However, upon SCF treatment, an increase in GSK3β phosphorylation in PCs becomes evident (Figures 6A and 6B). Western blot analysis of sorted *Lgr5*$^+$ and PCs confirmed the increased GSK3β phosphorylation in PCs, although not in CBC cells, upon DSS treatment (Figures 6C and 6D).

GSK3β inhibitory phosphorylation in SCF-treated PCs is expected to inhibit β-catenin proteolytic degradation, leading to its cytoplasmic accumulation and translocation into the nucleus, where it acts as a co-transcriptional factor to activate expression of Wnt target genes. To validate the ability of SCF to increase Wnt signaling even in already Wnt-active cells, the TOPflash/FOPflash (TOP/FOP) Wnt reporter gene assay was implemented in the colon cancer cell line CaCo2. Supplementation of the culture medium with recombinant SCF significantly enhanced Wnt signaling in this *APC* mutant cell line (Figure 6E). To validate that SCF can also activate Wnt signaling in PCs, qRT-PCR analysis of specific Wnt target genes was performed on sorted PCs treated with SCF. In line with the results of the reporter gene assay and in confirmation of the RNA-seq data from DSS-treated mice, upregulation of *Axin2*, *Jun*, and *Ccdn1* (cyclin D1) was found in SCF-treated PCs (Figure 6F).

To confirm that inflammation enhances Wnt signaling in PCs *in vivo*, we analyzed by IHC their intracellular β-catenin distribution. As expected, nuclear β-catenin was observed in PCs from control animals with hardly any cytoplasmic staining. In contrast, PCs from DSS-treated mice showed a clear increase in cytoplasmic β-catenin, indicative of its increased stability and, consequentially, of enhanced Wnt signaling (Figure 6G).

Because PC differentiation is known to be driven by Wnt (van Es et al., 2005), the functional consequences of its further activation downstream of the SCF/c-Kit signaling axis in a cell type already earmarked by nuclear β-catenin in the context of the regenerative response to inflammation are still unclear. To elucidate this aspect, we employed CHIR99021 (Chiron), a potent and selective GSK3β inhibitor leading to robust Wnt signaling activation, in organoid assays. As shown in Figures 6H and 6I, upon Chiron supplementation in the culture medium, PCs from control animals gave rise to high organoid numbers. As expected, Chiron treatment had a similar effect on *Lgr5*$^+$ CBC cells. Of note, although a majority of enterospheres (i.e., spherical structures primarily composed of stem cells and lacking budding and branching structures; Stelzner et al., 2012) were observed during the early phase of the culture, upon Chiron withdrawal, differentiation occurred, and "normal" organoid morphologies were observed both from PCs and *Lgr5*$^+$ cells (Figure 6I). Indeed, conversion between enterospheres and organoids has been shown to be regulated by Wnt signaling (Fordham et al., 2013; Mustata et al., 2013).

As shown previously (Figures 1D and 1E), mice treated with both DSS and ISCK03 suffered from increased loss of body weight and an overall decrease in DAI scores compared with animals treated with DSS alone. To assess whether this deleterious effect parallels the lack of Wnt "super-activation" downstream of the SCF/cKit signaling axis, β-catenin IHC analysis was again performed in small intestinal tissues from mice treated with DSS alone or in the presence of the ISCK03 inhibitor. As shown in Figure 7A, DSS treatment alone causes enhanced β-catenin accumulation in the cytoplasm and nucleus of PCs, indicative of increased Wnt signaling activation. This effect is almost entirely abrogated in mice treated simultaneously with both DSS and ISCK03. Furthermore, ISCK03 significantly reduced the number of Ki67$^+$ PCs in DSS-treated mice (Figures 7B and 7C and S7A). Accordingly, combined DSS/ISCK03 treatment of Lyz-Cre/YFP mice strongly compromised the ability of PCs to lineage-trace upon inflammation (Figures 7D and 7E).

(C) Western blot analysis of untreated and SCF-treated (50 ng/mL) *Lgr5*$^+$ and PCs using antibodies directed against c-Kit, phospho-GSK3β, total GSK3β, GFP, and actin.
(D) Quantification of phospho-GSK3β/GSK3β signal intensity in the western blot shown in (C) (*$p < 0.05$, n = 3; mean [SD] values are shown).
(E) TOP-Flash luciferase reporter assay of control and SCF-treated (50 ng/mL) CaCo2 cells (*$p < 0.05$, n = 3; mean [SD] values are shown).
(F) qRT-PCR analysis of control and SCF-treated (50 ng/mL) PCs using primer sets specific for the Wnt target genes Axin2, c-Jun, and Cyclin D1 (**$p < 0.01$, n = 3; mean [SD] values are shown).
(G) β-Catenin IHC analysis of intestinal tissues from control and 3% DSS-treated (7 days) mice 1 day after DSS withdrawal (arrows indicate PCs with increased cytoplasmic β-catenin; scale bars, 25 μm). Pictures show representative examples of crypts from 3 independent mouse experiments.
(H) Number of organoids derived from control or Chiron-treated (10 μM) *Lgr5*$^+$ or PCs sorted by FACS (***$p < 0.005$, n = 3; mean [SD] values are shown).
(I) Representative pictures of organoids derived from control and Chiron-treated (10 μM) *Lgr5*$^+$ or PCs sorted by FACS. Left: untreated cells did not give rise to organoids. Center: Chiron-treated Lgr5$^+$ and PCs generate enterospheres. Right: upon Chiron withdrawal, enterospheres give rise to differentiated enteroids.

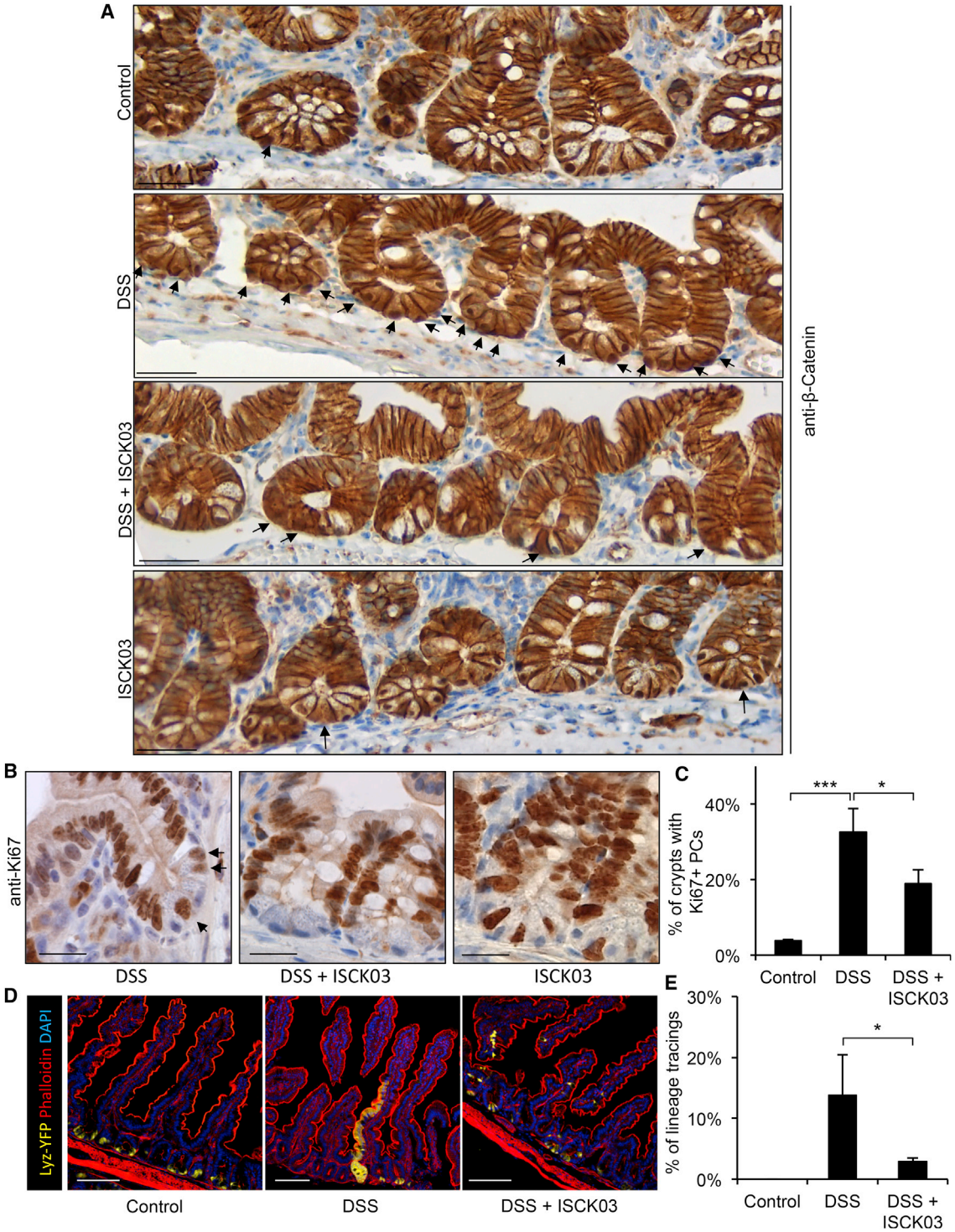

Figure 7. SCF/c-Kit Signaling Inhibition Counteracts DSS-Induced Wnt Activation and PC De-differentiation

(A) β-Catenin IHC analysis of intestinal tissues from control and DSS-, ISCK03-, or DSS + ISCK03-treated mice 1 day after stop of treatment (arrows indicate PCs with increased cytoplasmic β-catenin; scale bar, 25 μm). Pictures show representative examples of crypts from 3 independent mice.

(B) Ki67 immunohistochemistry analysis of intestinal tissues from control and DSS-, ISCK03-, or DSS + ISCK03-treated mice 1 day after stop of treatment (arrows indicate Ki67-expressing PCs; scale bars, 25 μm). Pictures show representative examples of crypts from 3 independent mice.

(legend continued on next page)

Taken together, these results show that inhibition of the SCF/c-Kit signaling axis prevents downstream Wnt signaling activation in PCs, compromising their capacity to acquire stem-like feature and to contribute to the regenerative response of the intestinal epithelium to the inflammatory insult.

DISCUSSION

IBD is regarded as an emerging global ailment in view of its steadily rising incidence during the last decades (M'Koma, 2013). Apart from its profound negative effects on the patient's quality of life, IBD is associated with an increased risk of developing intestinal cancer (Itzkowitz and Yio, 2004; Jia et al., 2008; Rosen and Jordan, 2009). From this perspective, the elucidation of the cellular and molecular mechanisms underlying the regenerative response of the intestinal stem cell niche to inflammatory tissue damage is of fundamental and translational relevance. Because of the complexity of the tissue response to injury and in view of the fact that IBD syndromes such as UC and CD affect different segments of the digestive tract, we have here chosen to model intestinal inflammation in the mouse through DSS administration in the drinking water (Elsheikh et al., 2012). The mucosal injury caused by DSS results in acute inflammation of the entire gastrointestinal (GI) tract (pan-gastroenteritis) through recruitment and activation of inflammatory cells, followed by a rapid tissue regeneration phase (Vowinkel et al., 2004), providing a useful preclinical *in vivo* inflammation model for both UC and CD. Although many other experimental (i.e., genetic) models for IBD exist that possibly better reflect the immune features of CD and UC, our choice for the DSS model is based on the similar predisposition of these mice to intestinal cancer, as observed in IBD (of high relevance when it comes to the stem cell origin of cancer), and by the ease and suitability of DSS administration to study the primary regenerative response of the stem cell niche to the tissue insult. Therefore, it does represent an ideal model to perform PC lineage tracing upon the primary inflammatory stimulus.

Enhanced secretion of the SCF has been reported in the plasma of IBD patients (Andersson et al., 2017; Comar et al., 2012) and confirmed here both in the intestinal epithelium and underlying stroma of UC and CD patients and in the DSS mouse model. This is of interest in view of the specific expression of the SCF transmembrane receptor c-Kit in PCs and their equivalent in the colon (Rothenberg et al., 2012). Increased SCF expression was also observed in intestinal epithelial cells in response to cholera toxin or *Salmonella enterica* Typhimurium infection (Klimpel et al., 1995, 1996). SCF/c-Kit signaling is a major regulator of proliferation and differentiation in the hematopoietic system (Broudy, 1997). Mast cells and dendritic cells express high *c-Kit* levels even when fully differentiated but retain the capacity to re-enter the cell cycle in response to extracellular SCF stimulation (Metcalfe et al., 1997; Ray et al., 2010). Besides, functional analysis of the response of PCs to SCF, as shown here, is of broader interest, as indicated by the role played by SCF expression from differentiated tumor cells in the maintenance of c-Kit-expressing colon cancer stem cells (Fatrai et al., 2015).

We here show that severe loss of *Lgr5*$^+$ CBC cells characterizes the primary response to DSS-driven inflammation. Targeted ablation of *Lgr5*$^+$ stem cells in the mouse intestinal epithelium showed that these cells are, in fact, dispensable and that their role is taken over by their quiescent counterparts (Tian et al., 2011; van der Flier et al., 2009b). Depletion of *Lgr5*$^+$ stem cells has also previously been reported in the colon of DSS-treated mice, where they reappear on day 5 of the recovery phase to then reach normal levels 1 day thereafter (Davidson et al., 2012). Similarly, loss of *Lgr5*$^+$ CBC cells has been observed upon high-dose γ-irradiation (Yan et al., 2012). In both cases, the depletion is temporary, and the CBC cell pool at the base of the crypt is rapidly restored.

More persistent CBC cell loss upon tissue injury is compensated by the regenerative response of alternative stem cell pools, including the infrequently cycling *Bmi1*$^+$ stem cells at position +4 (Sangiorgi and Capecchi, 2008; Yan et al., 2012) and secretory (*Dll1*$^+$) (van Es et al., 2012) and enterocyte (*Alpi*$^+$) (Tetteh et al., 2016) progenitors in addition to label retaining cells (LRCs) expressing PC markers (Buczacki et al., 2013; Roth et al., 2012), capable of reacquiring proliferative and self-renewal cell capacity upon tissue injury or targeted CBC cell ablation. Therefore, the intestinal epithelium shows remarkable plasticity, with several stem and progenitors cell types contributing to the restoration of tissue integrity and re-establishment of the actively cycling *Lgr5*$^+$ CBC cells (Yousefi et al., 2017). However, the ablation and tissue injury protocols employed in these studies are not directly relevant for IBD and the tissue damage caused by inflammation. Also, it is not clear whether the plasticity of the intestinal epithelium, apart from the above stem and progenitor cells, also extends to more committed and even post-mitotic lineages. Here we show that, following the initial loss of *Lgr5*$^+$ CBC cells, the response to acute inflammation features fully differentiated PCs capable of re-entering the cell cycle, losing their secretory features, and acquiring self-renewal and pluripotency, contributing to the repair and regeneration of the damaged intestinal tissue.

As mentioned above, the specific expression of the c-Kit receptor in PCs and in their counterparts in the colon (Rothenberg et al., 2012; Schewe et al., 2016) and the increased secretion of its natural ligand SCF upon inflammation both in IBD patients and in the DSS mouse model are of functional relevance for cell cycle re-entry, dedifferentiation, and acquisition of stem cell properties by these mature and normally post-mitotic secretory cells. Stimulation of the SCF/c-Kit signaling axis results in a cascade of downstream events from PI3/Akt pathway activation to GSK3β inhibitory phosphorylation. Of note, PI3K/Akt activation upon SCF/c-kit signaling induction has been shown to

(C) Quantification of the percentage of crypts with Ki67$^+$ PC in intestinal tissues of control, DSS-, and DSS + ISCK03-treated mice (*$p < 0.05$, ***$p < 0.005$, $n = 3$; mean [SD] values are shown).

(D) Lineage tracing analysis of tamoxifen-injected Lyz-Cre-R26-LSL-YFP mice (left, control; center, DSS; right, DSS + ISCK03). Tissues were harvested and analyzed 7 days after removal of DSS (scale bars, 100 μm).

(E) Quantification of PC lineage tracing events of the mice described in (D) ($n = 4$, *$p < 0.05$; mean [SD] values are shown).

promote cell proliferation, growth, and survival in several models, including colon cancer cell lines (Jeon et al., 2009; Vajravelu et al., 2015; Yasuda et al., 2007). Among the many pleiotropic effects of GSK3β inhibition, Wnt/β-catenin signaling activation is likely to play a central role in conferring proliferative and stem-like features to PCs, as observed here. However, it is well- established that Wnt signaling also underlies PC differentiation (van Es et al., 2005) and is retained in mature secretory cells, as indicated by their characteristic nuclear β-catenin staining. Distinct Wnt signaling dosages are associated with different downstream target genes and stem cell differentiation outcomes, as shown previously by our laboratory (Gaspar and Fodde, 2004; Kielman et al., 2002). Moreover, ectopic activation of canonical Wnt signaling has been shown to be essential for the quiescence exit of *mTert*$^+$ stem cells as well as for *Dll1*$^+$ progenitors to regain stemness (Montgomery et al., 2011; van Es et al., 2012). Indeed, *ex vivo* enhancement of Wnt signaling in PCs by GSK3β inhibition results in de novo organoid formation, highlighting the central role of the super-activation of this pathway downstream the SCF/c-Kit axis in the de-differentiation and cell cycle re-entry of secretory cells during tissue regeneration. Nonetheless, in view of the pleiotropic effects of Gsk3β inhibition on a broad spectrum of downstream signaling cascades, it is likely that other pathways synergize with Wnt in inducing PC dedifferentiation upon SCF/c-Kit activation. Recently, Yu et al. (2018) published a study confirming our original observations according to which PCs de-differentiate upon whole-body irradiation (12 Gy) (Roth et al., 2012). Of note, activation of Notch signaling, but not Wnt, seems to characterize the acquisition of stem-like features by PCs. In our RNA-seq analysis of PCs from DSS-treated mice, only very few of the differentially upregulated genes are indeed indicative of increased Notch signaling. Of the 12 genes reported in the study by Yu et al. (2018) as upregulated in PCs upon high-dose irradiation, only 4 (*Notch1*, *Dtx4*, *Hes1*, and *Rps19*) were significantly upregulated in our data. In view of the fact that *Hes1* has previously been reported as a Wnt target and *Notch1* as an activator of the Wnt pathway (Collu et al., 2014), it is likely that the well-established cross-talk between these two signaling pathways also comes into play upon inflammation. Nonetheless, it appears that Wnt signaling activation downstream of SCF/c-Kit and Gsk3β inhibition plays a central role in the observed de-differentiation of PCs upon inflammation, as functionally validated by several independent experimental approaches. Interestingly, Yu et al. (2018) employed an inducible mutant β-catenin allele to confirm that activation of Wnt did not play a central role in the dedifferentiation of PCs. However, this mutant allele is a potent oncogene resulting in extremely high Wnt signaling levels, the dosage of which may not be "just right" for the acquisition of stem-like features by PCs (Gaspar and Fodde, 2004). As mentioned above, it is plausible that, in view of the pleiotropic effects of Gsk3β inhibition, several other signaling pathways, including Notch, are activated and synergize with Wnt in this process.

The regenerative capacity of PCs is maintained *ex vivo,* as shown by their capacity to form small intestinal organoids when isolated from DSS-treated mice (or upon SCF stimulation) in the absence of *Lgr5*$^+$ CBC cells. Thus, PCs represent an additional pool of reserve stem cells capable of contributing to tissue regeneration upon injury. However, in view of their role in supporting *Lgr5*$^+$ CBC cells (Sato et al., 2011), it is also plausible that inflammatory cues may enhance their niche function next to expansion of the stem cell pool. Although *ex vivo* reconstitution of PCs from DSS-treated animals with *Lgr5*$^+$ CBC cells from control mice resulted in a marked increase in organoid multiplicity, analysis of their expression profiles did not reveal a significant increase in the expression of niche signals (e.g., EGF, transforming growth factor [TGF], Wnt3, or Dll4; data not shown) usually provided by PCs to maintain stemness of CBC cells (Sato et al., 2011). Nevertheless, inflammation is likely to exert context-dependent effects in the small and large intestine. Indeed, SCF was found among the proteins shown previously to be present at significantly different abundances between UC and CD (Andersson et al., 2017). PC metaplasia (i.e., the appearance of PCs in the colon, where they normally do not belong; Paterson and Watson, 1961), is frequently observed among UC patients and may result from differentiation of *c-Kit*$^+$ cells to provide further niche support to stem cells in response to inflammation. On the other end, metaplastic PCs have also been observed in colon adenomas and carcinomas (Lewin, 1968; Wada et al., 1992) and have been proposed to represent important precursors of IBD-associated colon cancer (Wada, 2009; Wada et al., 2005). Hence, the regenerative response to inflammatory tissue damage may differ between the small intestine and colon and reflect the distinct predisposition to bowel cancer among IBD patients. Lineage tracing of the *c-Kit*$^+$ Paneth-like cells of the colon upon DSS administration will likely clarify this aspect.

The presence of multiple and distinct pools of low-cycling stem cells in the intestinal epithelium raises the issue of their individual roles and relative contributions to tissue regeneration upon inflammation. Two studies showed that PC depletion does not have major consequences and, therefore, may be dispensable in intestinal tissue homeostasis and regeneration (Durand et al., 2012; Garabedian et al., 1997). However, it is unclear whether the ablation of PCs in these mouse models is limited to fully mature cells because their secretory precursors may compensate for the loss of niche and stem cell functions. Also, these depletion models have not been challenged by inflammation. In support of their essential role, other studies demonstrated that PCs are critical to provide niche support and maintain the *Lgr5*$^+$ stem cell population during crypt regeneration (Geiser et al., 2012; Parry et al., 2013; Sato et al., 2011). Given these rather controversial observations, future studies should focus on the role of PCs in ensuring intestinal tissue integrity, particularly in the context of inflammation. Notably, inhibition of SCF/c-Kit signaling resulted in increased weight loss and DAI upon inflammation, likely to result at least partially from the prevention of PCs to take part in intestinal tissue repair. However, because c-Kit is expressed in other cell types regulating inflammatory responses, such as mast, dendritic, and interstitial cells of Cajal (Miettinen and Lasota, 2005), further studies are required to reveal the specific role of c-Kit inhibition of PCs in the response to inflammation.

In conclusion, we show that activation of the SCF/c-Kit signaling axis upon inflammation induces cell cycle re-entry,

dedifferentiation, and acquisition of stem cell properties in PCs by enhancing Wnt through PI3K/Akt activation and GSK3β inhibition. Therefore, beside their role as regulators of the intestinal microflora and as niche cells for actively cycling CBC cells, PCs serve as a pool of quiescent stem cells that can be reactivated upon tissue insults and contribute to tissue regeneration. The diversity and complexity of their functional roles in IBD, dysbiosis, and cancer make Paneth(-like) cells in the small bowel and colon a central node for intestinal homeostasis and diseases.

STAR★METHODS

Detailed methods are provided in the online version of this paper and include the following:

- KEY RESOURCES TABLE
- CONTACT FOR REAGENT AND RESOURCE SHARING
- EXPERIMENTAL MODEL AND SUBJECT DETAILS
- METHOD DETAILS
  - Tamoxifen administration
  - DSS and ISCK03 treatment
  - Immunohistochemistry (IHC) analysis
  - Immunofluorescence (IF) and lineage tracing analysis
  - RNA *in situ* hybridization (ISH)
  - Organoid assays
  - *Ex vivo* lineage tracing
  - IF analysis of whole-mount intestinal crypts
  - Western blot analysis
  - FACS quantification and analysis of $Lgr5^{+}$-, Paneth-, and YFP^{+} cells by
  - TOP/FOP reporter assay
  - RNA isolation, RNA sequencing and quantitative real-time PCR
- QUANTIFICATION AND STATISTICAL ANALYSES
- DATA AND SOFTWARE AVAILABILITY

SUPPLEMENTAL INFORMATION

Supplemental Information includes seven figures and can be found with this article online at https://doi.org/10.1016/j.celrep.2018.07.085.

ACKNOWLEDGMENTS

This study was made possible by funding from the Dutch Cancer Society (KWF) (EMCR 2012-5473), the Netherlands Institute of Regenerative Medicine (NIRM) (http://www.nirmresearch.nl/index.html), and the World Cancer Research Funds (WCRF) (2014/1181).

AUTHOR CONTRIBUTIONS

M. Schewe and M. Schmitt were responsible for the study concept and design; data acquisition, analysis, and interpretation; and manuscript revision. A.S., D.F., W.S.v.d.G., M.T., H.F.S., R.J., M.E.v.R., H.J.G.v.d.W., J.v.E., and H.C. were responsible for data acquisition, analysis, and interpretation. R.F. was responsible for the study concept and design; data analysis and interpretation; manuscript writing and revision; obtaining funding; and study supervision.

DECLARATION OF INTEREST

The authors declare no competing interests.

Received: May 17, 2018
Revised: July 2, 2018
Accepted: July 25, 2018
Published: August 28, 2018

REFERENCES

Adolph, T.E., Tomczak, M.F., Niederreiter, L., Ko, H.J., Böck, J., Martinez-Naves, E., Glickman, J.N., Tschurtschenthaler, M., Hartwig, J., Hosomi, S., et al. (2013). Paneth cells as a site of origin for intestinal inflammation. Nature *503*, 272–276.

Andersson, E., Bergemalm, D., Kruse, R., Neumann, G., D'Amato, M., Repsilber, D., and Halfvarson, J. (2017). Subphenotypes of inflammatory bowel disease are characterized by specific serum protein profiles. PLoS ONE *12*, e0186142.

Barker, N., van Es, J.H., Kuipers, J., Kujala, P., van den Born, M., Cozijnsen, M., Haegebarth, A., Korving, J., Begthel, H., Peters, P.J., and Clevers, H. (2007). Identification of stem cells in small intestine and colon by marker gene Lgr5. Nature *449*, 1003–1007.

Barnett, S.F., Defeo-Jones, D., Fu, S., Hancock, P.J., Haskell, K.M., Jones, R.E., Kahana, J.A., Kral, A.M., Leander, K., Lee, L.L., et al. (2005). Identification and characterization of pleckstrin-homology-domain-dependent and isoenzyme-specific Akt inhibitors. Biochem. J. *385*, 399–408.

Bolger, A.M., Lohse, M., and Usadel, B. (2014). Trimmomatic: a flexible trimmer for Illumina sequence data. Bioinformatics *30*, 2114–2120.

Broudy, V.C. (1997). Stem cell factor and hematopoiesis. Blood *90*, 1345–1364.

Buczacki, S.J., Zecchini, H.I., Nicholson, A.M., Russell, R., Vermeulen, L., Kemp, R., and Winton, D.J. (2013). Intestinal label-retaining cells are secretory precursors expressing Lgr5. Nature *495*, 65–69.

Clevers, H. (2016). Modeling Development and Disease with Organoids. Cell *165*, 1586–1597.

Clevers, H.C., and Bevins, C.L. (2013). Paneth cells: maestros of the small intestinal crypts. Annu. Rev. Physiol. *75*, 289–311.

Collu, G.M., Hidalgo-Sastre, A., and Brennan, K. (2014). Wnt-Notch signalling crosstalk in development and disease. Cell. Mol. Life Sci. *71*, 3553–3567.

Comar, M., Secchiero, P., De Lorenzo, E., Martelossi, S., Tommasini, A., and Zauli, G. (2012). JCV+ Patients with Inflammatory bowel disease show elevated plasma levels of MIG and SCF. Inflamm. Bowel Dis. *18*, 1194–1196.

Cooper, H.S., Murthy, S.N., Shah, R.S., and Sedergran, D.J. (1993). Clinicopathologic study of dextran sulfate sodium experimental murine colitis. Lab. Invest. *69*, 238–249.

Dahlen, D.D., Lin, N.L., Liu, Y.C., and Broudy, V.C. (2001). Soluble Kit receptor blocks stem cell factor bioactivity in vitro. Leuk. Res. *25*, 413–421.

Davidson, L.A., Goldsby, J.S., Callaway, E.S., Shah, M.S., Barker, N., and Chapkin, R.S. (2012). Alteration of colonic stem cell gene signatures during the regenerative response to injury. Biochim. Biophys. Acta *1822*, 1600–1607.

Dobin, A., Davis, C.A., Schlesinger, F., Drenkow, J., Zaleski, C., Jha, S., Batut, P., Chaisson, M., and Gingeras, T.R. (2013). STAR: ultrafast universal RNA-seq aligner. Bioinformatics *29*, 15–21.

Doble, B.W., and Woodgett, J.R. (2003). GSK-3: tricks of the trade for a multitasking kinase. J. Cell Sci. *116*, 1175–1186.

Dubreuil, P., Letard, S., Ciufolini, M., Gros, L., Humbert, M., Castéran, N., Borge, L., Hajem, B., Lermet, A., Sippl, W., et al. (2009). Masitinib (AB1010), a potent and selective tyrosine kinase inhibitor targeting KIT. PLoS ONE *4*, e7258.

Durand, A., Donahue, B., Peignon, G., Letourneur, F., Cagnard, N., Slomianny, C., Perret, C., Shroyer, N.F., and Romagnolo, B. (2012). Functional intestinal stem cells after Paneth cell ablation induced by the loss of transcription factor Math1 (Atoh1). Proc. Natl. Acad. Sci. USA *109*, 8965–8970.

Edgar, R., Domrachev, M., and Lash, A.E. (2002). Gene Expression Omnibus: NCBI gene expression and hybridization array data repository. Nucleic Acids Res. *30*, 207–210.

Elsheikh, W., Flannigan, K.L., McKnight, W., Ferraz, J.G., and Wallace, J.L. (2012). Dextran sulfate sodium induces pan-gastroenteritis in rodents: implications for studies of colitis. J. Physiol. Pharmacol. *63*, 463–469.

Fatrai, S., van Schelven, S.J., Ubink, I., Govaert, K.M., Raats, D., Koster, J., Verheem, A., Borel Rinkes, I.H., and Kranenburg, O. (2015). Maintenance of Clonogenic KIT(+) Human Colon Tumor Cells Requires Secretion of Stem Cell Factor by Differentiated Tumor Cells. Gastroenterology *149*, 692–704.

Fordham, R.P., Yui, S., Hannan, N.R., Soendergaard, C., Madgwick, A., Schweiger, P.J., Nielsen, O.H., Vallier, L., Pedersen, R.A., Nakamura, T., et al. (2013). Transplantation of expanded fetal intestinal progenitors contributes to colon regeneration after injury. Cell Stem Cell *13*, 734–744.

Fuchs, E. (2009). The tortoise and the hair: slow-cycling cells in the stem cell race. Cell *137*, 811–819.

Garabedian, E.M., Roberts, L.J., McNevin, M.S., and Gordon, J.I. (1997). Examining the role of Paneth cells in the small intestine by lineage ablation in transgenic mice. J. Biol. Chem. *272*, 23729–23740.

Gaspar, C., and Fodde, R. (2004). APC dosage effects in tumorigenesis and stem cell differentiation. Int. J. Dev. Biol. *48*, 377–386.

Geiser, J., Venken, K.J., De Lisle, R.C., and Andrews, G.K. (2012). A mouse model of acrodermatitis enteropathica: loss of intestine zinc transporter ZIP4 (Slc39a4) disrupts the stem cell niche and intestine integrity. PLoS Genet. *8*, e1002766.

Grün, D., Muraro, M.J., Boisset, J.C., Wiebrands, K., Lyubimova, A., Dharmadhikari, G., van den Born, M., van Es, J., Jansen, E., Clevers, H., et al. (2016). De Novo Prediction of Stem Cell Identity using Single-Cell Transcriptome Data. Cell Stem Cell *19*, 266–277.

Itzkowitz, S.H., and Yio, X. (2004). Inflammation and cancer IV. Colorectal cancer in inflammatory bowel disease: the role of inflammation. Am. J. Physiol. Gastrointest. Liver Physiol. *287*, G7–G17.

Jeon, S., Kim, N.H., Kim, J.Y., and Lee, A.Y. (2009). Stem cell factor induces ERM proteins phosphorylation through PI3K activation to mediate melanocyte proliferation and migration. Pigment Cell Melanoma Res. *22*, 77–85.

Jia, Q., Lupton, J.R., Smith, R., Weeks, B.R., Callaway, E., Davidson, L.A., Kim, W., Fan, Y.Y., Yang, P., Newman, R.A., et al. (2008). Reduced colitis-associated colon cancer in Fat-1 (n-3 fatty acid desaturase) transgenic mice. Cancer Res. *68*, 3985–3991.

Kielman, M.F., Rindapää, M., Gaspar, C., van Poppel, N., Breukel, C., van Leeuwen, S., Taketo, M.M., Roberts, S., Smits, R., and Fodde, R. (2002). Apc modulates embryonic stem-cell differentiation by controlling the dosage of beta-catenin signaling. Nat. Genet. *32*, 594–605.

Klimpel, G.R., Chopra, A.K., Langley, K.E., Wypych, J., Annable, C.A., Kaiserlian, D., Ernst, P.B., and Peterson, J.W. (1995). A role for stem cell factor and c-kit in the murine intestinal tract secretory response to cholera toxin. J. Exp. Med. *182*, 1931–1942.

Klimpel, G.R., Langley, K.E., Wypych, J., Abrams, J.S., Chopra, A.K., and Niesel, D.W. (1996). A role for stem cell factor (SCF): c-kit interaction(s) in the intestinal tract response to Salmonella typhimurium infection. J. Exp. Med. *184*, 271–276.

Lennartsson, J., and Rönnstrand, L. (2012). Stem cell factor receptor/c-Kit: from basic science to clinical implications. Physiol. Rev. *92*, 1619–1649.

Lewin, K. (1968). Neoplastic Paneth cells. J. Clin. Pathol. *21*, 476–479.

Li, N., Yousefi, M., Nakauka-Ddamba, A., Jain, R., Tobias, J., Epstein, J.A., Jensen, S.T., and Lengner, C.J. (2014). Single-cell analysis of proxy reporter allele-marked epithelial cells establishes intestinal stem cell hierarchy. Stem Cell Reports *3*, 876–891.

Liao, Y., Smyth, G.K., and Shi, W. (2014). featureCounts: an efficient general purpose program for assigning sequence reads to genomic features. Bioinformatics *30*, 923–930.

Love, M.I., Huber, W., and Anders, S. (2014). Moderated estimation of fold change and dispersion for RNA-seq data with DESeq2. Genome Biol. *15*, 550.

M'Koma, A.E. (2013). Inflammatory bowel disease: an expanding global health problem. Clin. Med. Insights Gastroenterol. *6*, 33–47.

Metcalfe, D.D., Baram, D., and Mekori, Y.A. (1997). Mast cells. Physiol. Rev. *77*, 1033–1079.

Miettinen, M., and Lasota, J. (2005). KIT (CD117): a review on expression in normal and neoplastic tissues, and mutations and their clinicopathologic correlation. Appl. Immunohistochem. Mol. Morphol. *13*, 205–220.

Montgomery, R.K., Carlone, D.L., Richmond, C.A., Farilla, L., Kranendonk, M.E., Henderson, D.E., Baffour-Awuah, N.Y., Ambruzs, D.M., Fogli, L.K., Algra, S., and Breault, D.T. (2011). Mouse telomerase reverse transcriptase (mTert) expression marks slowly cycling intestinal stem cells. Proc. Natl. Acad. Sci. USA *108*, 179–184.

Muñoz, J., Stange, D.E., Schepers, A.G., van de Wetering, M., Koo, B.K., Itzkovitz, S., Volckmann, R., Kung, K.S., Koster, J., Radulescu, S., et al. (2012). The Lgr5 intestinal stem cell signature: robust expression of proposed quiescent '+4' cell markers. EMBO J. *31*, 3079–3091.

Mustata, R.C., Vasile, G., Fernandez-Vallone, V., Strollo, S., Lefort, A., Libert, F., Monteyne, D., Pérez-Morga, D., Vassart, G., and Garcia, M.I. (2013). Identification of Lgr5-independent spheroid-generating progenitors of the mouse fetal intestinal epithelium. Cell Rep. *5*, 421–432.

Na, Y.J., Baek, H.S., Ahn, S.M., Shin, H.J., Chang, I.S., and Hwang, J.S. (2007). [4-t-butylphenyl]-N-(4-imidazol-1-yl phenyl)sulfonamide (ISCK03) inhibits SCF/c-kit signaling in 501mel human melanoma cells and abolishes melanin production in mice and brownish guinea pigs. Biochem. Pharmacol. *74*, 780–786.

Orford, K.W., and Scadden, D.T. (2008). Deconstructing stem cell self-renewal: genetic insights into cell-cycle regulation. Nat. Rev. Genet. *9*, 115–128.

Parry, L., Young, M., El Marjou, F., and Clarke, A.R. (2013). Evidence for a crucial role of paneth cells in mediating the intestinal response to injury. Stem Cells *31*, 776–785.

Paterson, J.C., and Watson, S.H. (1961). Paneth cell metaplasia in ulcerative colitis. Am. J. Pathol. *38*, 243–249.

Potten, C.S. (1998). Stem cells in gastrointestinal epithelium: numbers, characteristics and death. Philos. Trans. R. Soc. Lond. B Biol. Sci. *353*, 821–830.

Ray, P., Krishnamoorthy, N., Oriss, T.B., and Ray, A. (2010). Signaling of c-kit in dendritic cells influences adaptive immunity. Ann. N Y Acad. Sci. *1183*, 104–122.

Rosen, J.M., and Jordan, C.T. (2009). The increasing complexity of the cancer stem cell paradigm. Science *324*, 1670–1673.

Roth, S., and Fodde, R. (2011). Quiescent stem cells in intestinal homeostasis and cancer. Cell Commun. Adhes. *18*, 33–44.

Roth, S., Franken, P., Sacchetti, A., Kremer, A., Anderson, K., Sansom, O., and Fodde, R. (2012). Paneth cells in intestinal homeostasis and tissue injury. PLoS ONE *7*, e38965.

Rothenberg, M.E., Nusse, Y., Kalisky, T., Lee, J.J., Dalerba, P., Scheeren, F., Lobo, N., Kulkarni, S., Sim, S., Qian, D., et al. (2012). Identification of a cKit(+) colonic crypt base secretory cell that supports Lgr5(+) stem cells in mice. Gastroenterology *142*, 1195–1205.e6.

Sangiorgi, E., and Capecchi, M.R. (2008). Bmi1 is expressed in vivo in intestinal stem cells. Nat. Genet. *40*, 915–920.

Sasaki, N., Sachs, N., Wiebrands, K., Ellenbroek, S.I., Fumagalli, A., Lyubimova, A., Begthel, H., van den Born, M., van Es, J.H., Karthaus, W.R., et al. (2016). Reg4+ deep crypt secretory cells function as epithelial niche for Lgr5+ stem cells in colon. Proc. Natl. Acad. Sci. USA *113*, E5399–E5407.

Sato, T., Vries, R.G., Snippert, H.J., van de Wetering, M., Barker, N., Stange, D.E., van Es, J.H., Abo, A., Kujala, P., Peters, P.J., and Clevers, H. (2009). Single Lgr5 stem cells build crypt-villus structures in vitro without a mesenchymal niche. Nature *459*, 262–265.

Sato, T., van Es, J.H., Snippert, H.J., Stange, D.E., Vries, R.G., van den Born, M., Barker, N., Shroyer, N.F., van de Wetering, M., and Clevers, H. (2011). Paneth cells constitute the niche for Lgr5 stem cells in intestinal crypts. Nature *469*, 415–418.

Schewe, M., and Fodde, R. (2018). Multitasking Paneth cells in the intestinal stem cell niche. In Advances in Stem Cells and their Niches, D. Bonnet, ed. (Elsevier), pp. 41–75.

Schewe, M., Franken, P.F., Sacchetti, A., Schmitt, M., Joosten, R., Böttcher, R., van Royen, M.E., Jeammet, L., Payré, C., Scott, P.M., et al. (2016). Secreted Phospholipases A2 Are Intestinal Stem Cell Niche Factors with Distinct Roles in Homeostasis, Inflammation, and Cancer. Cell Stem Cell *19*, 38–51.

Schewe, M., Sacchetti, A., Schmitt, M., and Fodde, R. (2017). The Organoid Reconstitution Assay (ORA) for the Functional Analysis of Intestinal Stem and Niche Cells. J. Vis. Exp. (Published online November 20, 2017. https://doi.org/10.3791/56329.

Schmieder, R., and Edwards, R. (2011). Quality control and preprocessing of metagenomic datasets. Bioinformatics *27*, 863–864.

Stelzner, M., Helmrath, M., Dunn, J.C., Henning, S.J., Houchen, C.W., Kuo, C., Lynch, J., Li, L., Magness, S.T., Martin, M.G., et al.; NIH Intestinal Stem Cell Consortium (2012). A nomenclature for intestinal in vitro cultures. Am. J. Physiol. Gastrointest. Liver Physiol. *302*, G1359–G1363.

Tarasov, A., Vilella, A.J., Cuppen, E., Nijman, I.J., and Prins, P. (2015). Sambamba: fast processing of NGS alignment formats. Bioinformatics *31*, 2032–2034.

Tetteh, P.W., Basak, O., Farin, H.F., Wiebrands, K., Kretzschmar, K., Begthel, H., van den Born, M., Korving, J., de Sauvage, F., van Es, J.H., et al. (2016). Replacement of Lost Lgr5-Positive Stem Cells through Plasticity of Their Enterocyte-Lineage Daughters. Cell Stem Cell *18*, 203–213.

Tian, H., Biehs, B., Warming, S., Leong, K.G., Rangell, L., Klein, O.D., and de Sauvage, F.J. (2011). A reserve stem cell population in small intestine renders Lgr5-positive cells dispensable. Nature *478*, 255–259.

Vajravelu, B.N., Hong, K.U., Al-Maqtari, T., Cao, P., Keith, M.C., Wysoczynski, M., Zhao, J., Moore, J.B., 4th, and Bolli, R. (2015). C-Kit Promotes Growth and Migration of Human Cardiac Progenitor Cells via the PI3K-AKT and MEK-ERK Pathways. PLoS ONE *10*, e0140798.

van der Flier, L.G., Haegebarth, A., Stange, D.E., van de Wetering, M., and Clevers, H. (2009a). OLFM4 is a robust marker for stem cells in human intestine and marks a subset of colorectal cancer cells. Gastroenterology *137*, 15–17.

van der Flier, L.G., van Gijn, M.E., Hatzis, P., Kujala, P., Haegebarth, A., Stange, D.E., Begthel, H., van den Born, M., Guryev, V., Oving, I., et al. (2009b). Transcription factor achaete scute-like 2 controls intestinal stem cell fate. Cell *136*, 903–912.

van Es, J.H., Jay, P., Gregorieff, A., van Gijn, M.E., Jonkheer, S., Hatzis, P., Thiele, A., van den Born, M., Begthel, H., Brabletz, T., et al. (2005). Wnt signalling induces maturation of Paneth cells in intestinal crypts. Nat. Cell Biol. *7*, 381–386.

van Es, J.H., Sato, T., van de Wetering, M., Lyubimova, A., Yee Nee, A.N., Gregorieff, A., Sasaki, N., Zeinstra, L., van den Born, M., Korving, J., et al. (2012). Dll1+ secretory progenitor cells revert to stem cells upon crypt damage. Nat. Cell Biol. *14*, 1099–1104.

Vowinkel, T., Kalogeris, T.J., Mori, M., Krieglstein, C.F., and Granger, D.N. (2004). Impact of dextran sulfate sodium load on the severity of inflammation in experimental colitis. Dig. Dis. Sci. *49*, 556–564.

Wada, R. (2009). Proposal of a new hypothesis on the development of colorectal epithelial neoplasia: nonspecific inflammation–colorectal Paneth cell metaplasia–colorectal epithelial neoplasia. Digestion *79* (*Suppl 1*), 9–12.

Wada, R., Miwa, H., Abe, H., Santo, R.M., Kitamura, S., Kuwabara, N., Suda, K., Kondo, K., Yamada, S., Hamada, T., et al. (1992). Incidence of Paneth cells in minute tubular adenomas and adenocarcinomas of the large bowel. Acta Pathol. Jpn. *42*, 579–584.

Wada, R., Yamaguchi, T., and Tadokoro, K. (2005). Colonic Paneth cell metaplasia is pre-neoplastic condition of colonic cancer or not? J. Carcinog. *4*, 5.

Wen, P.Y., Lee, E.Q., Reardon, D.A., Ligon, K.L., and Alfred Yung, W.K. (2012). Current clinical development of PI3K pathway inhibitors in glioblastoma. Neuro-oncol. *14*, 819–829.

Yan, K.S., Chia, L.A., Li, X., Ootani, A., Su, J., Lee, J.Y., Su, N., Luo, Y., Heilshorn, S.C., Amieva, M.R., et al. (2012). The intestinal stem cell markers Bmi1 and Lgr5 identify two functionally distinct populations. Proc. Natl. Acad. Sci. USA *109*, 466–471.

Yasuda, A., Sawai, H., Takahashi, H., Ochi, N., Matsuo, Y., Funahashi, H., Sato, M., Okada, Y., Takeyama, H., and Manabe, T. (2007). Stem cell factor/c-kit receptor signaling enhances the proliferation and invasion of colorectal cancer cells through the PI3K/Akt pathway. Dig. Dis. Sci. *52*, 2292–2300.

Yilmaz, O.H., Katajisto, P., Lamming, D.W., Gültekin, Y., Bauer-Rowe, K.E., Sengupta, S., Birsoy, K., Dursun, A., Yilmaz, V.O., Selig, M., et al. (2012). mTORC1 in the Paneth cell niche couples intestinal stem-cell function to calorie intake. Nature *486*, 490–495.

Yousefi, M., Li, L., and Lengner, C.J. (2017). Hierarchy and Plasticity in the Intestinal Stem Cell Compartment. Trends Cell Biol. *27*, 753–764.

Yu, S., Tong, K., Zhao, Y., Balasubramanian, I., Yap, G.S., Ferraris, R.P., Bonder, E.M., Verzi, M.P., and Gao, N. (2018). Paneth Cell Multipotency Induced by Notch Activation following Injury. Cell Stem Cell *23*, 46–59.e5.

STAR★METHODS

KEY RESOURCES TABLE

REAGENT or RESOURCE	SOURCE	IDENTIFIER
Antibodies		
Rabbit-anti SCF	Rockland	600-401-EE1; RRID: AB_2613750
Goat anti-GFP (Biotin)	Genetex	GTX26658; RRID: AB_371422
Rabbit anti-Ki-67/Mki67	Novus biologicals	NB500-170; RRID: AB_10001977
Goat anti-Lysozyme (clone C19)	Santa Cruz	sc-27958; RRID: AB_2138790
Rabbit anti-Lysozyme EC 3.2.1.17	Dako	A0099; RRID: AB_2341230
Rabbit anti-Muc2	Santa Cruz	sc-15334; RRID: AB_2146667
Rabbit anti-chromogranin A	Novus Biologicals	NB120-15160; RRID: AB_789299
Rabbit anti-DCAMKL1	Abcam	ab31704; RRID: AB_873537
Rabbit anti-phospho-GSK3β (Ser9) (clone 5B3)	Cell signaling	9323; RRID: AB_2115201
Rabbit anti-Gsk3β (clone D5C5Z)	Cell signaling	12456; RRID: AB_2636978
Rabbit anti-phospho-Akt (Ser473)	Cell signaling	9271; RRID: AB_329825
Mouse anti-Akt (pan) (clone 40d4)	Cell signaling	2920; RRID: AB_1147620
Rabbit anti-c-Kit (clone D13A2)	Cell signaling	3074; RRID: AB_1147633
Rabbit anti-OLFM4 (clone D6Y5A)	Cell signaling	39141; RRID: AB_2650511
Rabbit anti-β-actin (clone D6A8)	Cell signaling	8457; RRID: AB_10950489
Mouse anti-β-catenin (clone 14/BETA-CATENIN)	BD Biosciences	610154; RRID: AB_397555
Rabbit anti-CD3	Abcam	ab5690; RRID: AB_305055
APC-conjugated anti-mouse CD24 antibody (clone M1/69)	Biolegend	101814; RRID: AB_439716
Brilliant Violet 421 Rat anti-mouse TER-119/Erythroid Cells (clone TER-119)	Biolegend	563998
Brilliant Violet 421 Rat anti-mouse CD31 (clone 390),	Biolegend	563356
Brilliant Violet 421 Rat anti-mouse CD45 (clone 30-F11)	Biolegend	563890; RRID: AB_2651151
PE Rat anti-mouse CD117 (c-Kit) Antibody (clone 2B8)	Biolegend	105808; RRID: AB_313217
Goat anti-Rabbit IgG (H+L) secondary Antibody, Alexa Fluor® 568 conjugate	Life Technologies	A-11011; RRID: AB_143157
Donkey anti-Rabbit IgG (H+L) secondary Antibody, Alexa Fluor® 568 conjugate	Life Technologies	A-21202; RRID: AB_141607
Donkey anti-Goat secondary Antibody, Alexa Fluor® 633 conjugate	Life Technologies	A-21082; RRID: AB_2535739
Goat anti-Rabbit IgG (H+L) Secondary Antibody, HRP	ThermoFisher	A16096; RRID: AB_2534770
Goat anti-Mouse IgG (H+L) Secondary Antibody, HRP	ThermoFisher	A16066; RRID: AB_2534739
Biological Samples		
Human intestinal tissues	Archive of the department of Pathology at the Erasmus MC	anonymous
Chemicals, Peptides, and Recombinant Proteins		
Tamoxifen	Sigma	T5648
Sun flower oil	Sigma	S5007
Dextran sulfate sodium (colitis grade)	MP Biomedicals	0216011050
ISCK03	Cayman Chemical	15781
SCF	Peprotech	250-03
Bovine Serum Albumin (BSA)	Sigma	A9647-100G
Skim Milk powder for microbiology	Merck Millipore	1.15363.0500
Recombinant Mouse CD117/c-kit Fc Chimera Protein (soluble c-kit receptor)	R&D Systems	1356-SR-050
Y-27632	Sigma	Y0503

(*Continued on next page*)

Continued

REAGENT or RESOURCE	SOURCE	IDENTIFIER
B27	gibco	12587-010
N-2 Supplement	gibco	17502-048
Recombinant mouse EGF	gibco	PMG8041
Noggin	Peprotech	250-38
Jagged1	AnaSpec	61298
Masitinib	Selleckchem	S1064
Chiron (CHIR99021)	Tocris	4423
NVP-BKM120	Cayman Chemical	11587
AKT inhibitor VIII	Cayman Chemical	14870
Rapamycin	Cayman Chemicals	13346
U0126	Cayman Chemicals	70970
LY294002	Cayman Chemicals	70920
Ruxolitinib	Cayman Chemicals	11609
KP cryocompound	Klinipath	1620-C
VECTASHIELD HardSet Antifade Mounting Medium	Vector Labs	H-1400
Matrigel	Corning	356231
Fugene HD	Promega	N/A
TRIzol™ Reagent	ThermoFisher	15596018
Alexa Fluor® 568 Phalloidin	Invitrogen	A12380
Alexa Fluor® 633 Phalloidin	Invitrogen	A22284
DAPI	Sigma	D8417
Hoechst 34580	ThermoFisher	H21486
HRP-Streptavidin Conjugate	Invitrogen	43-4323
Advanced DMEM/F12 medium	gibco	12634-010
TrypLE Express	gibco	12605-010
Deoxyribonuclease 1 from bovine pancreas (DNase)	Sigma	DN25
Pertex	Histolab	00811
4% buffered formaldehyde solution (Klinipath)	Klinipath	VWRK4078-9010
Critical Commercial Assays		
Rabbit EnVision+ System-HRP	Dako	K4011
Mouse EnVision+ System-HRP	Dako	K4007
RNAscope kit	ACDbio	323200
Pierce ECL Western Blotting Substrate	ThermoFisher	32106
Agilent RNA 6000 Pico Kit	Agilent Technologies	5067-1513
Taqman®PreAmp Master Mix	Applied Biosystems	4391128
High Capacity RNA-to-cDNA kit (Applied Biosystems)	Applied Biosystems	4387406
Deposited Data		
Raw and analyzed data	This paper	GEO: GSE117216
Experimental Models: Cell Lines		
Cell line: Caco-2 [Caco2] (ATCC® HTB-37)	American Type Culture Collection	http://www.atcc.org/Products/All/HTB-37.aspx?geo_country=us
Experimental Models: Organisms/Strains		
Mouse: pLys^{CreERT2}	Clevers laboratory	https://www.hubrecht.eu/research-groups/clevers-group/
Mouse: B6.Cg-*Gt(ROSA)26Sor*$^{tm14(CAG-tdTomato)Hze}$/J	Jackson laboratory	https://www.jax.org/strain/007914
Mouse: B6.129X1-*Gt(ROSA)26Sor*$^{tm1(EYFP)Cos}$/J	Jackson laboratory	https://www.jax.org/strain/006148
Mouse: B6.129P2-*Lgr5*$^{tm1(cre/ERT2)Cle}$/J	Jackson laboratory	https://www.jax.org/strain/008875
Mouse: JAX C57BL/6J Mice	Charles River	https://www.jax.org/strain/000664

(*Continued on next page*)

Continued

REAGENT or RESOURCE	SOURCE	IDENTIFIER
Oligonucleotides		
SCF mRNA (RNAscope® 2.5 VS Probe- Mm-Kitl)	ACDbio	423409
RNAscope® 2.5 VS Positive Control Probe- Bt-PPIB	ACDbio	319459
Axin2 Mm00443610_m1	ThermoFisher	433182
Actb Mm02619580_g1	ThermoFisher	433182
Ccnd1 Mm00432359_m1	ThermoFisher	433182
Jun Mm00495062_s1	ThermoFisher	433182
Recombinant DNA		
M50 Super 8x TOPFlash	Addgene	12456
M51 Super 8x FOPFlash (TOPFlash mutant)	Addgene	12457
pRL-TK renilla	Promega	
Software and Algorithms		
Fiji software	N/A	https://fiji.sc/

CONTACT FOR REAGENT AND RESOURCE SHARING

Further information and requests for reagents may be directed to and will be fulfilled by the Lead Contact, Riccardo Fodde at Erasmus Medical Center Rotterdam, Email: R.Fodde@erasmusmc.nl.

EXPERIMENTAL MODEL AND SUBJECT DETAILS

All mice employed in this study were aged between 8-12 weeks of age, fed *ad libitum*, and maintained on a 12-hour light/dark cycle at the Erasmus MC animal facility (EDC) and the IPMC animal facility under conventional SPF conditions. Inbred C57BL/6J mice were from Charles River Laboratories. *Lgr5*$^{EGFP\text{-}IRES\text{-}creERT2}$, *R26*$^{LSL\text{-}YFP}$ and *R26*$^{LSL\text{-}tdTomato}$ mice were from Jackson laboratories. All mice used in this study were on a C57BL/6J background.

The generation and characterization of the *Lys*^{CreERT2}/*R26*$^{LSL\text{-}YFP}$ model will be described elsewhere (J.v.E., unpublished data). In short: the pLys^{CreERT2} mouse model was generated through homologous recombination in IB10 embryonic stem cells (129/Ola). The CreERT2 gene was knocked onto the ATG start codon of the of the lysozyme (*Lys*) gene. Both flanking arms were generated by high-fidelity PCR reactions from male 129/Ola-derived BAC DNA and subsequently cloned into PL451. The targeting construct (100 μg) was linearized and transfected into male 129/Ola-derived IB10 embryonic stem cells by electroporation (800V, 3F). Recombinant ES cell clones expressing the neomycin gene were selected in medium supplemented with G418 (250 μg/ml). Recombinant embryonic stem cell clones were screened by Southern blotting. The frequency of homologous recombination was 4%. Two positive clones were selected and injected into C57BL/6 derived blastocysts using standard procedures. Both injected clones gave germline transmission. The neomycin selection cassette was flanked by Frt recombination sites and excised *in vivo* by crossing the mice with the general FLP deleter strain (Jackson Lab.). *Lys*^{CreERT2} mice were then crossed with R26$^{LSL\text{-}YFP}$ mice (R26R-YFP, #006148, Jackson Lab). All procedures were approved by local (Erasmus MC ''Instantie voor Dierenwelzijn'' and ''Dierenexperimentencommissie'') and national (Centrale Commissie Dierproeven) review and performed in agreement with local animal welfare laws and guidelines.

METHOD DETAILS

Tamoxifen administration

To activate C-recombinase, *Lgr5*$^{EGFP\text{-}IRES\text{-}creERT2}$/*R26*$^{LSL\text{-}RFP}$ mice were intraperitoneally (i.p) injected once with 1mg/20 g body-weight of Tamoxifen (Sigma); the *Lys*^{CreERT2}/*R26*$^{LSL\text{-}YFP}$ were i.p. injected three times on consecutive days with 1 mg/20 g body weight. Tamoxifen was dissolved in 100% Ethanol (stock concentration 200mg/ml). For i.p. injection the Tamoxifen stock solution was diluted 1:10 in sunflower oil (Sigma). As controls, mice were injected with 10% Ethanol in sunflower oil.

DSS and ISCK03 treatment

Mice were administered 3% dextran sulfate sodium salt (colitis-grade; MP Biomedicals) through the drinking water for seven days during which the animals were monitored for a specific set of parameters including stool consistency, blood loss, appearance, and % weight loss. DAI scores upon DSS-induced inflammation were obtained according to (Cooper et al., 1993) with minor modifications. DAI scores were as follows: stool consistency = normal (0), loose (1), diarrhea (2); blood loss = no loss (0), gross bleeding (1); appearance = normal (0), hunched (1), starey coat (2), lethargic (3); % weight loss = none (0), 0-10 (2), 10-20 (2), > 20 (3). ISCK03 (#15781,

Cayman Chemical) was administered via drinking water to the mice at a concentration of 0.1 mg/ml. For lineage tracing experiments, IF, IHC, or RNA *in situ* hybridization (ISH) analysis, mice were sacrificed at indicated time points post DSS treatment.

Immunohistochemistry (IHC) analysis

Mouse tissues were fixed overnight in 4% PFA and embedded in paraffin. Human tissues (normal and IBD) were already available as paraffin blocks from the department of Pathology at the Erasmus MC. Four μm sections were mounted on slides. IHC was performed using antibodies against SCF (1:500; Rockland), OLFM4 (1:200; CST), Mki67 (1:200; Novus biologicals) β-catenin (1:500; BD Biosciences) and CD3 (1:400; Abcam). Briefly, paraffin embedded sections were dewaxed with Xylene and hydrated in 100% and 70% ethanol. Antigen retrieval was performed using pressure cooker pretreatment in a Tris-EDTA buffer (pH 9.0). Slides were then incubated at 25°C in 3% hydrogen peroxidase for 15' to block endogenous peroxidase activity. Tissue sections were washed and blocked with 5% BSA in PBS-Tween for 1 hour to then be incubated with the primary antibody overnight at 4°C. Slides were washed twice with PBS-Tween and incubated with Rabbit EnVision+ System-HRP (Dako) or Mouse EnVision+ System-HRP (Dako) for 30 min. Sections were counterstained with Mayer's Hematoxylin and dehydration was performed by incubation in 70% and 100% ethanol followed by Xylene, before slides were mounted using Pertex (Histolab). The quantification of Ki67$^+$ Paneth cells refers to the amount of crypts containing at least one Ki67+ PC was detected.

The quantification of Olfm4$^+$ cells is based on the average number of Olfm4-positive cells per crypt throughout the length of the small intestine. The quantification of CD3$^+$ cells is based on the average number of CD3$^+$ -positive cells infiltrating the intestinal epithelium per villus. For each quantification, at least 50 crypts or villi per mouse, and at least 3 experimental mice were employed.

Immunofluorescence (IF) and lineage tracing analysis

Paraffin embedded tissues were prepared as described for IHC up to the peroxidase blocking step. For cryo-sections, tissue samples were first dissected and washed with PBS, to then be fixed for 2 hours at 25°C with 4% buffered formaldehyde solution (Klinipath). Tissues were cryo-protected in 30% sucrose (Sigma) overnight at 4°C, embedded in OCT (KP cryocompound, Klinipath), frozen on dry ice, and sectioned at −20°C. Tissues were cut in 4-8 μm thick sections. When applicable, sections were incubated in blocking buffer (5% milk powder in PBS-T) for 30 min. at 25°C, and stained with primary antibodies directed against the following proteins: Mki67 (1:100; Novus biologicals), lysozyme (C19) (1:100; Santa Cruz), lysozyme EC 3.2.1.17 (1:1000; Dako), c-Kit (D13A2)(1:100; CST), OLFM4 (1:100; CST), Muc2 (H-300) (1:500; Santa Cruz), chromogranin A (1:200; Novus Biologicals), and DCAMKL1 (1:200; Abcam) in blocking buffer overnight at 4°C. After washing in PBS-T, slides were incubated for 2 hours with the following secondary antibodies: Goat anti-Rabbit IgG (H+L) secondary Antibody, Alexa Fluor® 568 conjugate, (1:250; Life Technologies), Donkey anti-Rabbit IgG (H+L) secondary Antibody, Alexa Fluor® 568 conjugate (1:250; Life technologies) or Donkey anti-Goat secondary Antibody, Alexa Fluor® 633 conjugate (1:250; Life technologies). Tissues were counterstained with Alexa Fluor® 568 Phalloidin (1:100; Invitrogen) or Alexa Fluor® 633 Phalloidin (1:100; Invitrogen), and DAPI (Sigma) for 30 min. at 25°C and washed in PBS-T. Tissues were mounted in VECTASHIELD HardSet Antifade Mounting Medium (Vector Labs) and imaged with a Zeiss LSM700 confocal microscope. Images were processed with ImageJ (U.S. National Institutes of Health, Bethesda, MD, USA).

Lineage tracing frequency of *Lys*^{CreERT2}/*R26*$^{LSL\text{-}YFP}$ was quantified by dividing the number of intestinal crypt/villus axes containing YFP$^+$ ribbons by YFP$^+$ crypts.

RNA *in situ* hybridization (ISH)

Paraffin embedded tissues were prepared as described for IHC. SCF ISH analysis was performed by using the RNAscope kit (ACDbio) according to the manufacturer's instructions. Four μm formalin-fixed, paraffin-embedded tissue sections were pretreated with heat and protease before hybridization with a target probe to SCF mRNA (RNAscope® 2.5 VS Probe- Mm-Kitl (ACDbio)). An HRP-based signal amplification system was then applied followed by colorimetric development with DAB. Positive staining was identified as brown, punctate dots. Specificity of the SCF-RNA probes were tested by using PPIB (Cyclophilin B) and DapB gene (ACDbio) as positive and negative controls, respectively.

Organoid assays

To establish organoid cultures *ex vivo*, two distinct sources of cells were employed namely either whole crypts or single cell suspensions both from freshly resected mouse intestinal tissues. Whole crypts were extracted from the small intestine by incubating the minced tissues with 2 mM EDTA for 30 min. at 4°C. Crypts were then pelleted and passed through a 70 μm strainer. Whole crypt cultures were performed as previously described in standard ENR medium (Sato et al., 2009) supplemented, when indicated, with SCF (150ng/ml; Peprotech), soluble c-kit receptor (500ng/ml; R&D Systems), masitinib (200nM; Selleckchem), rapamycin (10 nM; Cayman Chemicals), U0126 (1 μM; Cayman Chemicals), LY294002 (5 μM; Cayman Chemicals),and ruxolitinib (0.5 μM; Cayman Chemicals).

As for organoid reconstitution assays (ORA), isolated crypts were first digested to single cells after incubation with TrypLE (Life Technologies) and 2000 U/ml-1 Dnase (Sigma) for 10 min. at 37°C. Dissociated cells were passed through a 40 μm strainer, stained with an APC-conjugated CD24 antibody (clone M1/69 BioLegend), and, to exclude non-epithelial cells, with the following Ab's for 30 min. at 4°C: BV421-conjugated TER119 (Biolegend), CD31 (Biolegend), CD45 (Biolegend). For PC analysis, an additional staining with a PE-conjugated CD117 antibody (Biolegend) was also performed. Cells were then sorted by FACS (BD FACSAriaIII;

BD Bioscience). Single viable epithelial cells were gated by CD24 and side scatter (SSC), and by negative selection against the above BV421-conjugated Ab's and with DAPI to discriminate live from dead cells. Detailed FACS gating strategy for the small intestine was performed as previously described (Roth et al., 2012). Reconstitution of *Lgr5*-EGFP^{hi} stem cells (purity > 99%) with PCs (CD24hiSSChi; purity > 98%) was performed by pelleting sorted cells at 300 g. for 5 minutes in Eppendorf LoBind Tubes, and by co-incubating them for 15 min. at 25°C as previously described (Sato et al., 2011). In order to implement the reconstitution assay upon activation of sorted cells with SCF, Paneth or *Lgr5*-EGFP^{hi} cells were first incubated with 150 ng/ml of recombinant murine SCF for 30 min. at 37°C in DMEM F12 before reconstitution. In order to inactivate GSK3β, sorted Paneth and *Lgr5*$^{+}$ cells were incubated with standard reconstitution medium + 5 μM Chiron (CHIR99021, Tocris) for 4 days followed by incubation in standard ENR medium. In order to inhibit PI3K and AKT, sorted PCs were incubated with specific chemical inhibitors NVP-BKM120 for PI3K (1 μM; Cayman Chemical) and AKT inhibitor VIII for AKT (4μM; Cayman Chemicals) for 30 min., centrifuged at 300 g for 5 min., and then washed in 200 μL of Advanced DMEM F12. Following these treatments, Paneth and *Lgr5*$^{+}$ stem cells were centrifuged at 300 g for 5 minutes and subsequently reconstituted by resuspension in 30 μL Matrigel (Corning), and culture in 96 Well Flat Bottom dishes (Corning). Alternatively, they were plated singularly where indicated. The composition of the culture medium was as previously described for whole crypts after supplementation with 10 μM Y-27632 (Sigma) and 1 mM Jagged-1 (AnaSpec). Brightfield pictures of organoids were taken using the Zeiss Primovert inverted microscope.

Ex vivo lineage tracing

Lys^{CreERT2}/*R26*$^{LSL-YFP}$ were treated with Tamoxifen as described above to induce Cre recombination. Mice were then either left untreated or treated with 3% DSS in drinking water for 7days. 3 days after removal of DSS, intestinal crypts were isolated, single cell digested and YFP^{+} cells within the PC gates (CD24^{hi}SSC^{hi}) were sorted by FACS. YFP^{+} PCs (n = 4000) were then plated in 30 μl Matrigel in a single well of a glass bottom 96 well plate and maintained at 37°C and 5% CO2. Culture medium (as described for the reconstitution assay) was changed every other day. For SCF treatments, YFP^{+} cells from control mice were either left untreated or treated with 150 ng/ml SCF for 30 min. before plating. Also in this case, culture medium (including 150 ng/ml SCF, for the SCF treated conditions) was replenished on a daily basis. At day 7, organoids were counterstained with 2μg/ml (Hoechst 34580) and imaged using a Zeiss CLSM510 Meta confocal microscope.

IF analysis of whole-mount intestinal crypts

Whole crypts were extracted from the small intestine by incubating the minced tissues with 2 mM EDTA for 30 min. at 4°C. Crypts were then pelleted and passed through a 70 μm strainer. Pelleted crypts were resuspended either in Advanced DMEM F12 or Advanced DMEM containing 50 ng/ml recombinant murine SCF ((#250-03, Peprotech), transferred to Eppendorf LoBind microcentrifuge tubes (Sigma) and incubated for 10 min. at 37°C. Subsequently, crypts were pelleted (300 g, 5 min. at 4°C) and fixed with 4% buffered formaldehyde solution (Klinipath) for 20 min. at 25°C. Crypts were washed twice with cold PBS and resuspended in block (5% milk powder in PBS-T) and incubated for 30 min. at 25°C. Afterward, the crypts were stained with primary antibodies against the following proteins: phospho-GSK3β (Ser9) (1:100; CST), Gsk3β (D5C5Z) (1:100; CST), phospho-Akt (Ser473)(1:100; CST), panAkt (40d4) (1:100; CST), lysozyme (C19) (1:100; Santa Cruz), in blocking buffer overnight at 4°C. After washing in PBS-T, slides were incubated for 2 hours with the following secondary antibodies: goat anti-rabbit IgG (H+L) secondary antibody, Alexa Fluor® 568 conjugate (1:250, Life Technologies), donkey anti-rabbit IgG (H+L) secondary antibody, Alexa Fluor® 568 conjugate (1:250, Life technologies) or donkey anti-goat secondary antibody, Alexa Fluor® 633 conjugate (1:250; Life technologies). Tissues were counterstained with Alexa Fluor® 568 Phalloidin (1:100; Invitrogen) or Alexa Fluor® 633 Phalloidin (1:100; Invitrogen) and DAPI (Sigma) for 30 min. at 25°C and washed in PBS-T. Crypts were then resuspended in VECTASHIELD HardSet Antifade Mounting Medium (Vector Labs), transferred to glass slides and covered with a coverslip. Images were taken with a Zeiss LSM700 confocal microscope and processed with ImageJ (U.S. National Institutes of Health, Bethesda, MD, USA). The relative phospho-GSK3β intensity of PCs was quantified by setting PCs as region of interest (ROI) and measuring the average intensity of the phospho-GSK3β signal within the ROI. PCs of at least 10 crypts per mouse per condition were analyzed.

Western blot analysis

Paneth and Lgr5-EGFP cells from C57BL/6J mice were extracted and FACS sorted as described for the organoid reconstitution assay. Sorted cells were incubated either in Advanced DMEM F12 medium or medium containing 50 ng/ml recombinant murine SCF (Peprotech) for 30 min. at 25°C. Subsequently, cells were lysed in RIPA lysis buffer (50 mM TrisHCl pH 7.5, 150 mM NaCl, 0.5% TritonX, 10% Glycerol, 10% DTT, and 1x NuPAGE LDS Sample Buffer (Life Technologies)). Lysates were subjected to standard SDS-PAGE and western blotting procedures using primary antibodies directed against c-Kit (D13A2)(1:1000; CST), phospho-Akt (Ser473) (1:1000; CST), panAkt (40d4) (1:2000; CST), phospho-GSK3β (Ser9) (1:1000; CST), Gsk3β (D5C5Z) (1:1000; CST), GFP (1:500; Genetex) and β-actin (D6A8) (1:1000; CST) and anti-Rabbit-HRP (1:1000), anti-Mouse-HRP (1:1000) secondary antibodies (Life Technologies) as well as HRP-Streptavidin Conjugate (1:1000; Invitrogen). Signal detection was performed by using the enhanced chemiluminescence system (ECL; Thermo Fisher Scientific, Schwerte, Germany) and the Molecular Imager® Gel Doc XR System (Bio-Rad). Protein bands were quantified using ImageJ (U.S. National Institutes of Health, Bethesda, MD, USA). pAkt and phospho-Gsk3β bands were normalized to the total Akt or Gsk3β bands, respectively, as well as to β-actin bands and fold values were calculated upon comparison with the negative background of the C57BL/6J lysates. As no significant differences between the

fold inductions of both ways of normalization was detected we used the normalization of phospho versus total protein bands as result in our manuscript.

FACS quantification and analysis of Lgr5^{+}-, Paneth-, and YFP^{+} cells by

Intestinal crypts from untreated or DS- treated *Lgr5*$^{EGFP\text{-}IRES\text{-}creERT2}$ or tamoxifen-injected *Lys*^{CreERT2}/*R26*$^{LSL\text{-}YFP}$ mice were isolated, single cell digested, and subjected to FACS analysis. *Lgr5*$^{+}$ and Paneth (CD24^{hi}SSC^{hi}) cells were identified and quantified by using previously established gates (Roth et al., 2012). For control or DSS treated *Lys*^{CreERT2}/*R26*$^{LSL\text{-}YFP}$ mice, YFP^{+} and YFP^{-} cells were identified as in Figure 4B, and the percentage of YFP^{+} and YFP^{-} cells within and outside the PC gate (CD24^{hi}SSC^{hi}) was quantified.

TOP/FOP reporter assay

For the β-catenin/TCF reporter assay (TOP-Flash assay), cells were plated on 24-well plates and, when 70% confluence was reached, transfected by Fugene HD (Promega) with 250 ng of the TOP-Flash or FOPFlash reporter constructs together with 25 ng of the Renilla luciferase vector for normalization purposes. SCF was added were indicated at 150ng/ml. Luciferase activity was measured by Dual–Luciferase Reporter Assay System (Promega) 48h post-transfection. Luminescence was measured using a Glomax Luminometer.

RNA isolation, RNA sequencing and quantitative real-time PCR

PCs [CD24hiSSChi] and *Lgr5*+ stem/progenitor cells derived from *Lgr5*-EGFP mice were sorted as described for the organoid reconstitution assay from crypt preparations of the small intestine and RNA was isolated from cells using TRIzol^{TM} Reagent (ThermoFisher Scientific) according to the manufacturer's instructions. RNA quality and quantity was evaluated on a 2100 Bio-analyzer (Agilent) using the Agilent RNA 6000 Pico Kit (Agilent Technologies). For RNA sequencing analysis, RNA samples were further processed by GATC-Biotech (Konstanz, Germany) according to the INVIEW^{TM} Transcriptome Explore library preparation protocol (Illumina based).

RNA-seq data of PC samples (n = 7) was performed using UCSC mouse genome build mm10 (reference strain C57BL/6J) and GENCODE annotation release M15 (GRCm38.p5). FASTQC (v0.11.5) (Schmieder and Edwards, 2011) was applied on the single-end FASTQ files for quality control, both before and after running trimmomatic (v0.36) (Bolger et al., 2014), which removed TrueSeq adaptor sequences. STAR (v2.5.3a) (Dobin et al., 2013) was used as aligner, with 2-pass mapping for each sample separately. Mapping quality plot was generated and checked based on sambamba Flagstat statistics (Tarasov et al., 2015). Count files, with the number of reads for each gene were created with subread FeatureCounts (1.5.2) (Liao et al., 2014). R (version 3.4.3) was used for further calculating statistics and data visualizations. Differential expression analysis were performed with condition 'DSS treatment' (n = 4) versus 'Control' (n = 3) using the DESeq2 package (v1.18.1) (Love et al., 2014) and the Wald-test. P values were adjusted using the Benjamini-Hochberg procedure. Heatmap visualization (Z-Scores averages per condition) was performed with the ggplot2 package (v2.1.0) on Regularized Log (from the DESeq2 package) transformed data and Z-Score were calculated with the base R 'scale' function (column scaling, followed by column centering). For quantitative RT-PCR purposes, RNA was converted into cDNA using the High Capacity RNA-to-cDNA kit (Applied Biosystems) and employed in a pre-amplification step using the Taqman®PreAmp Master Mix (Applied Biosystems) according to manufacturer's instructions. The linearity of the pre-amplification reaction was controlled for all primers. Assays were carried out as duplicate reactions using the 7500 Real Time system (Applied Biosystems). Finally, quantitative PCR was performed using inventoried TaqMan assays (Applied Biosystems) according to manufacturer's instructions. The *Actb* gene was employed as housekeeping gene. The assay number of the Taqman probes employed in this study for qRT-PCR purposes: Axin2 Mm00443610_m1, Actb Mm02619580_g1, Jun Mm00495062_s1, Ccnd1 Mm00432359_m1

QUANTIFICATION AND STATISTICAL ANALYSES

Statistical an graphical analyses was conducted using FIJI and Microsoft Excel 2016. The immunofluorescent and immunohistochemistry as well as *in situ* hybridization on mouse tissues were performed on at least 3 sections of at least 3 mice per experimental condition. Immunohistochemistry and Immunofluorescence on human tissues were performed on at least 3 sections from 2 healthy, 4 CD and 5 UC patients. Weight loss graphs and DAI scores where related to the following number of mice: treated with 3% DSS alone n = 6, ISCK03 alone n = 3, and 3% DSS + ISCK03 n = 6. All whole crypt organoid assays and ORA assays where plated in triplicates per condition and repeated at least 3 independent times. All FACS experiments were obtained from at least 3 mice per experimental condition.

For Figures 2A, 2B, S2A, S4A, and S4B, the FACS analyses were performed from cells of 5 independent mice per condition. In Figure 2B and Figure S4B, the average % of cells within the specified gates was quantified. In Figures 2D and 7D, the lineage tracing frequency of *Lgr5*$^{EGFP\text{-}IRES\text{-}creERT2}$/*R26*$^{LSL\text{-}RFP}$ and *Lys*^{CreERT2}/*R26*$^{LSL\text{-}YFP}$ was quantified by dividing the number of intestinal crypt/villus axes containing YFP^{+} ribbons by YFP^{+} crypts. At least 200 crypts per mouse of at least 3 experimental mice per condition were quantified. For Figure 2F, the average number of OLFM4+ cells per crypt of at least 50 crypts per mouse (n = 3 per condition) was quantified. For Figures 3B and 7C, the average percentage of crypts with at least one Ki67^{+} PC was quantified. At least 50 crypts per mouse of at least 3 independent mice per condition were analyzed. In Figures 5C and 6C, pAkt and phospho-Gsk3β bands were normalized to the total Akt or Gsk3β bands, respectively, as well as to β-actin bands and fold values were calculated upon comparison with the negative background of the C57BL/6J lysates. As no significant differences between the fold inductions of both ways of

normalization was detected, we used the normalization of phospho versus total protein bands as result in our manuscript. For Figure 6B, PCs were set as ROI (region of interest and the average intensity of the phospho-GSK3β signal within the ROI was measured. Results represent the average intensity of PCs of at least 30 crypts per mouse (n = 3/condition). Analysis was performed using the Fiji software. For Figure S1F, the quantification of $CD3^+$ cells is based on the average number of $CD3^+$ -positive cells infiltrating the intestinal epithelium per villus. For each quantification, at least 50 crypts or villi per mouse, and at least 3 experimental mice per condition were analyzed. Statistical comparisons between two groups were performed using unpaired two-tailed Student's t test and *p values* are indicated in the corresponding graphs. *p values* < 0.05 were considered as statistically significant. Error bars are indicated as MEAN (SD).

DATA AND SOFTWARE AVAILABILITY

The accession number for the RNA-seq data reported in this paper is GEO: GSE117216 (Edgar et al., 2002).

Cell Reports, Volume *24*

Supplemental Information

Paneth Cells Respond to Inflammation and Contribute to Tissue Regeneration by Acquiring Stem-like Features through SCF/c-Kit Signaling

Mark Schmitt, Matthias Schewe, Andrea Sacchetti, Danny Feijtel, Wesley S. van de Geer, Miriam Teeuwssen, Hein F. Sleddens, Rosalie Joosten, Martin E. van Royen, Harmen J.G. van de Werken, Johan van Es, Hans Clevers, and Riccardo Fodde

Supplementary Fig.1 (related to Fig. 1)

A

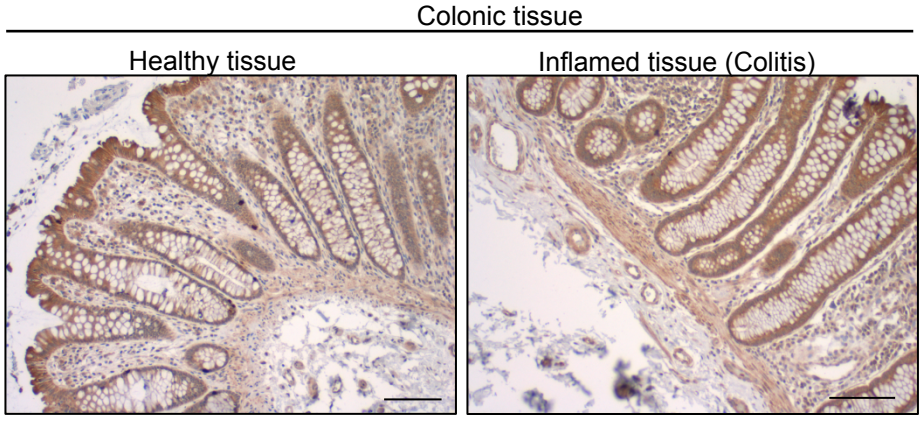

B

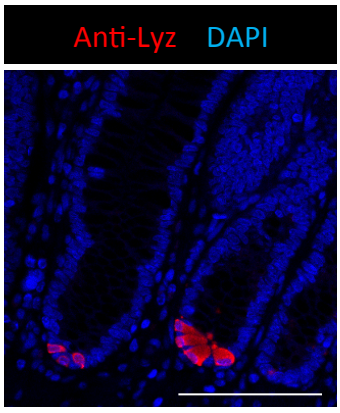

C

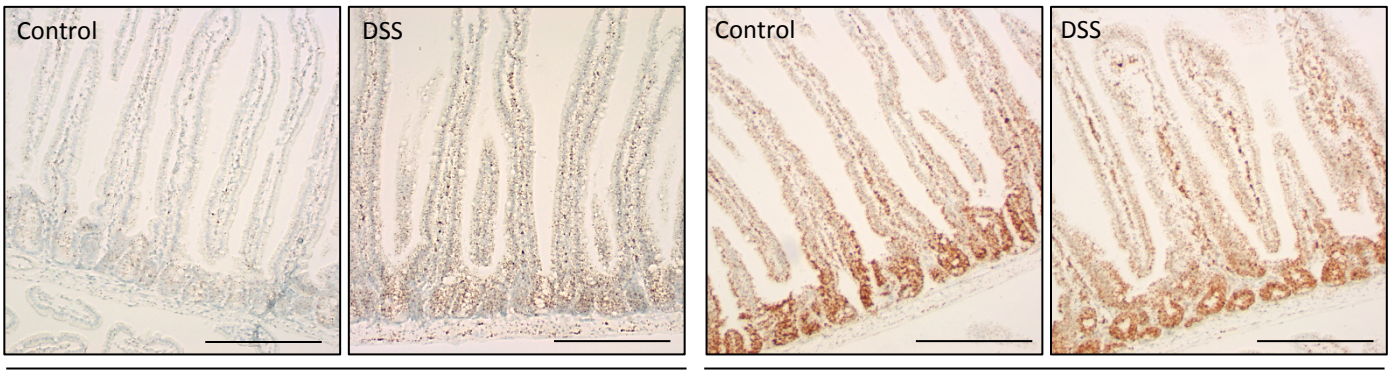

D

Mouse ID	Genotype	Treatment	Stool consistency (0-2)	Blood loss (0-1)	Appearance (0-3)	Weight loss (0-3)	DAI score
1	C57BL/6J	DSS	Diarrhea (2)	Gross bleeding (1)	Starey coat (2)	10,18% (2)	7
2	C57BL/6J	DSS	Loose (1)	No blood (0)	hunched (1)	10,75% (2)	4
3	C57BL/6J	DSS	Loose (1)	Gross bleeding (1)	hunched (1)	7,5% (1)	4
4	C57BL/6J	DSS	Loose (1)	No blood (0)	hunched (1)	9% (1)	3
5	C57BL/6J	DSS	Loose (1)	No blood (0)	Starey coat (2)	7,27% (1)	4
6	C57BL/6J	DSS	Diarrhea (2)	Gross bleeding (1)	Hunched (1)	10% (2)	6
7	C57BL/6J	DSS+ISCK03	Diarrhea (2)	Gross bleeding (1)	Lethargic (3)	20,3% (3)	9
8	C57BL/6J	DSS+ISCK03	Diarrhea (2)	Gross bleeding (1)	Starey coat (2)	22,5% (3)	8
9	C57BL/6J	DSS+ISCK03	Diarrhea (2)	Gross bleeding (1)	Lethargic (3)	16,73% (2)	8
10	C57BL/6J	DSS+ISCK03	Diarrhea (2)	Gross bleeding (1)	Starey coat (2)	16,96% (2)	7
11	C57BL/6J	DSS+ISCK03	Diarrhea (2)	Gross bleeding (1)	Lethargic (3)	19,91% (2)	8
12	C57BL/6J	DSS+ISCK03	Diarrhea (2)	Gross bleeding (1)	Lethargic (3)	19,52% (2)	8

E

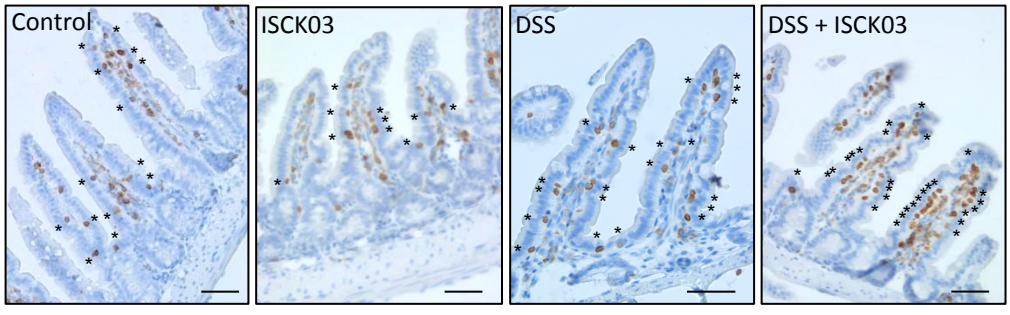

F

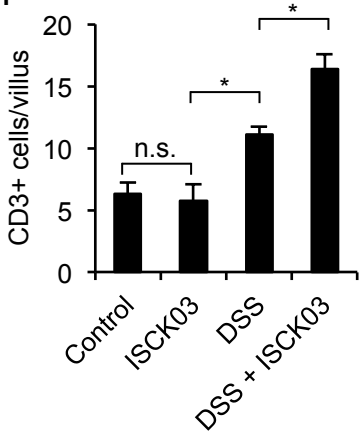

Supplementary Figure 1 (related to Figure 1)

A) Comparison of SCF expression of healthy colonic (left) and colonic tissues of patients with ulcerative colitis. Picture shows a representative example of 2 healthy and 5 UC patients (scale bars = 100 µm).

B) Lysozyme immunostaining of colonic tissues of patients with ulcerative colitis. Picture shows a representative example of metaplastic Paneth cells in the colon found in 3 out of 5 patients (scale bar = 100µm).

C) SCF RNA *in situ* hybridisation on small intestinal tissues of control (left) and DSS treated mice (right) 1 day after removal of DSS showing increased SCF RNA levels in the intestinal epithelium and submucosa of inflamed mice. PPIB RNA probes were used as positive controls. Pictures show representative examples of n= 3 mice; scale bar = 200µm).

D) Table of DAI scoring parameters of mice treated for 7 days with DSS or DSS + ISCK. Mice were sacrificed one day after stop of treatment. Mice treated with ISCK03 alone (n=3) did show normal stool consistency, no blood loss, normal appearance and no weight loss and were not included in the table.

E) CD3 immunhistochemistry analysis of intestinal tissues from control and DSS, ISCK03 or DSS + ISCK03 treated mice 1 day after stop of treatment (asterisks indicate infiltrating $CD3^+$ T-lymphocytes; scale bar = 50 µm).

F) Quantification of infiltrating $CD3^+$ T-lymphocytes/villus in control, DSS and DSS + ISCK03 treated mice described in A (*$p < 0.05$; n.s. = not significant; n=3).

Supplementary Fig. 2 (related to Fig. 2)

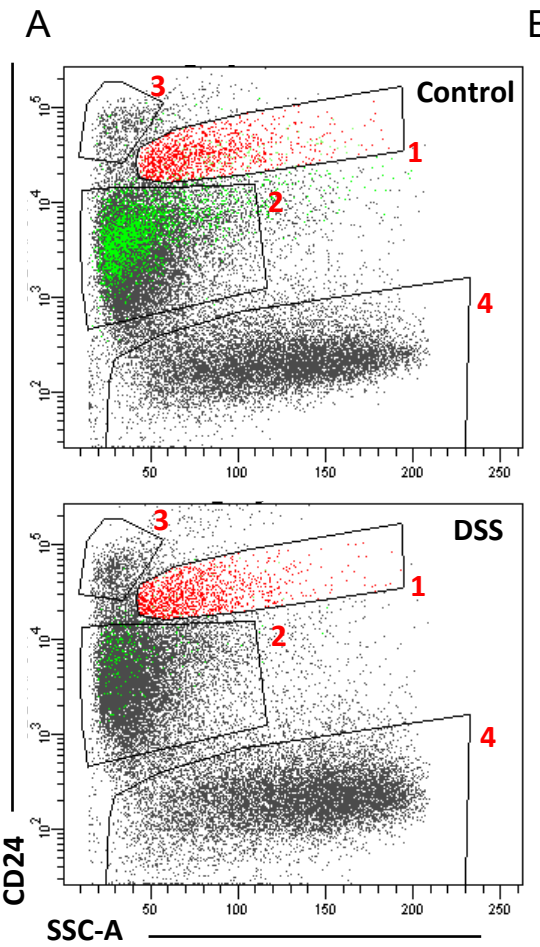

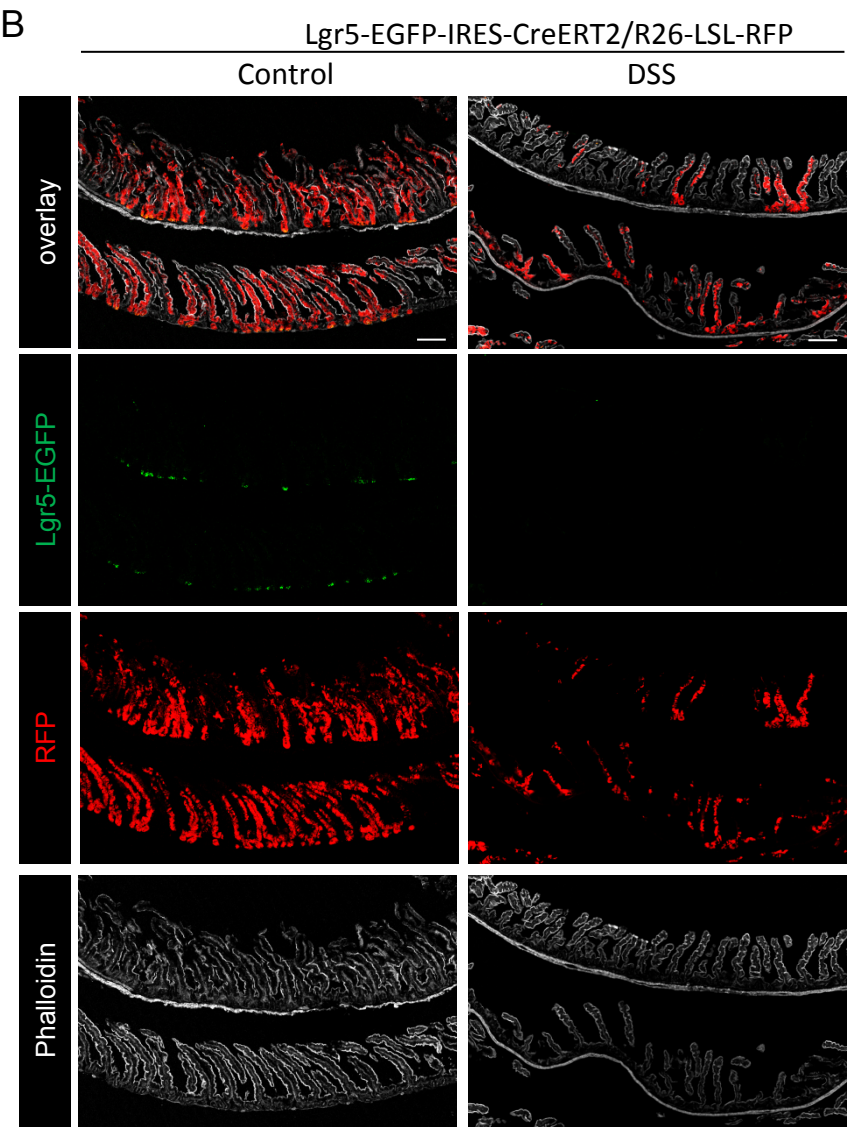

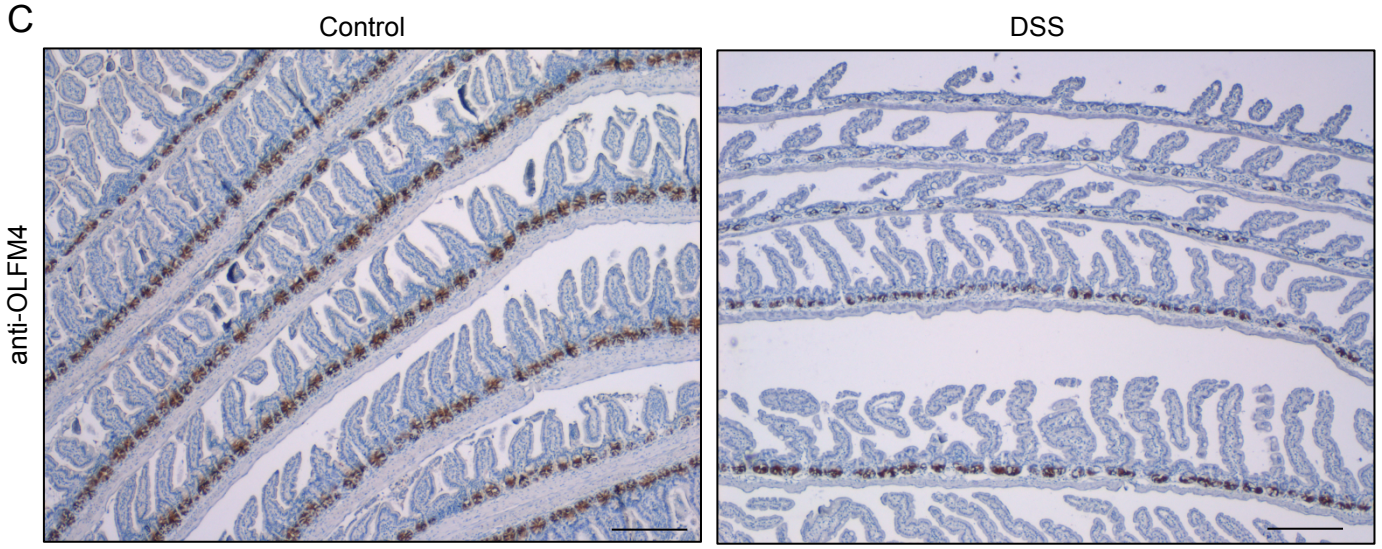

Supplementary Figure 2 (related to Figure 2)

A) FACS analysis of *Lgr5*$^{+}$ and Paneth cells (C24^{high}/SSC^{high}) in control or DSS treated mice 3 days after withdrawal of DSS (FACS plots are representrative of 5 independent experiments; cells within the Paneth cell gate are labelled in red; *Lgr5*-EGFP+ cells, as defined in Fig. 2A, are labelled in green).

B) Confocal microscopy images of small intestinal tissues of Tamoxifen treated *Lgr5*$^{-EGFP\text{-}IRES\text{-}CreERT2}$/R26$^{-LSL\text{-}RFP}$ mice subjected to normal drinking water or 3% DSS. Tissues were harvested 3 days after withdrawal of DSS. Picture shows an overview of *Lgr5* lineage tracings in small intestinal tissues (scale bar = 200 µm).

C) Olfm4 immunohistochemistry analysis of intestinal tissues from control and DSS treated mice 1 day after removal of DSS. Picture shows an overview of Olfm4 staining in small intestinal tissues (scale bar = 250 µm).

Supplementary Fig. 3 (related to Fig. 3)

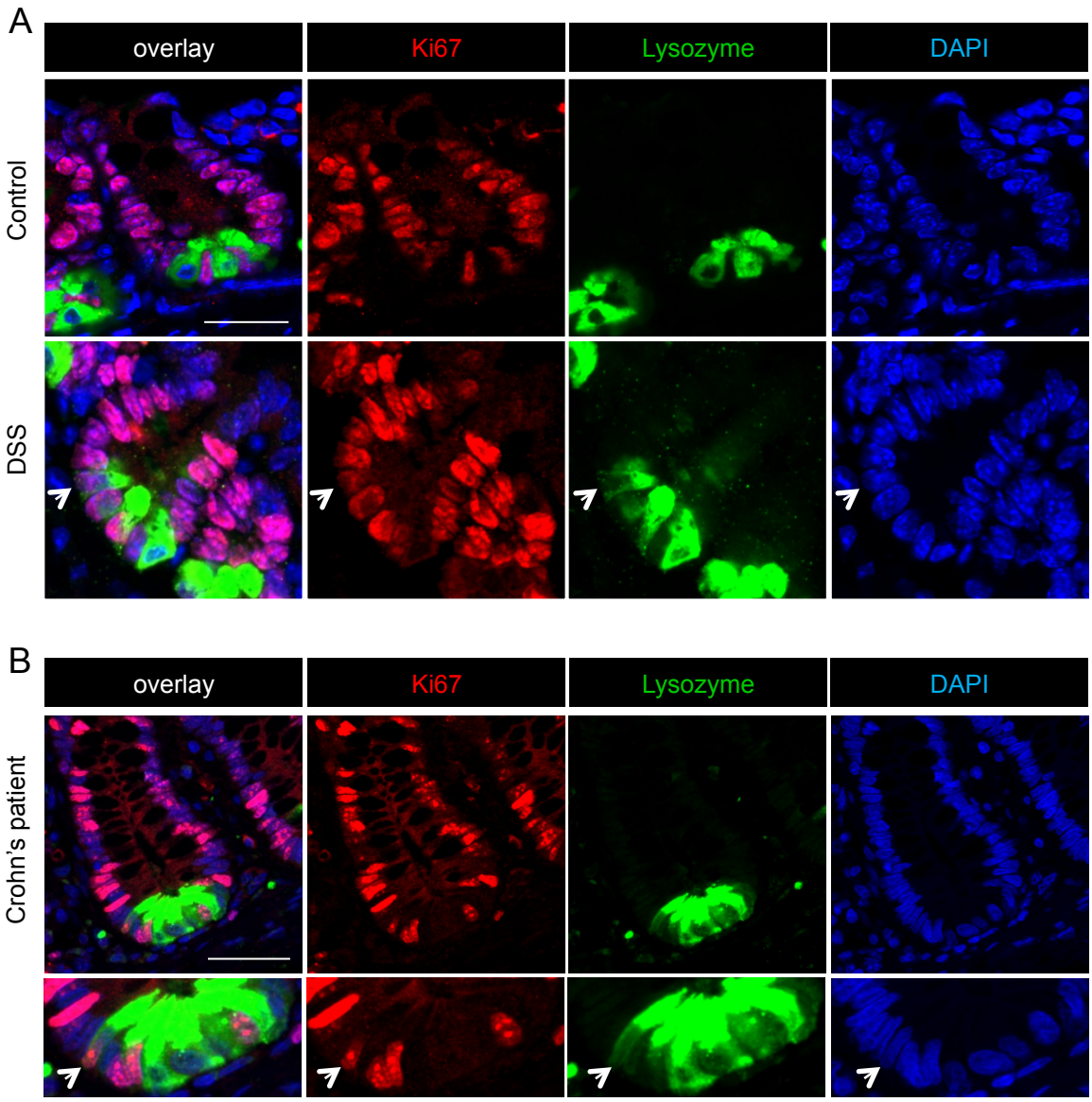

Supplementary Figure 3 (related to Figure 3)

A) Ki67/lysozyme double immunostaining of small intestinal tissues of untreated (upper panel) or DSS treated mice (lower panel). Tissues were harvested 1 day after DSS treatment (arrow indicates a Ki67/lysozyme double positive cell; scale bar = 25 μm)

B) Ki67/lysozyme double immunostaining of small intestinal tissues of a CD patient (arrow indicates a Ki67/lysozyme double positive cell; scale bar = 25 μm)

Supplementary Fig. 4 (related to Fig. 4)

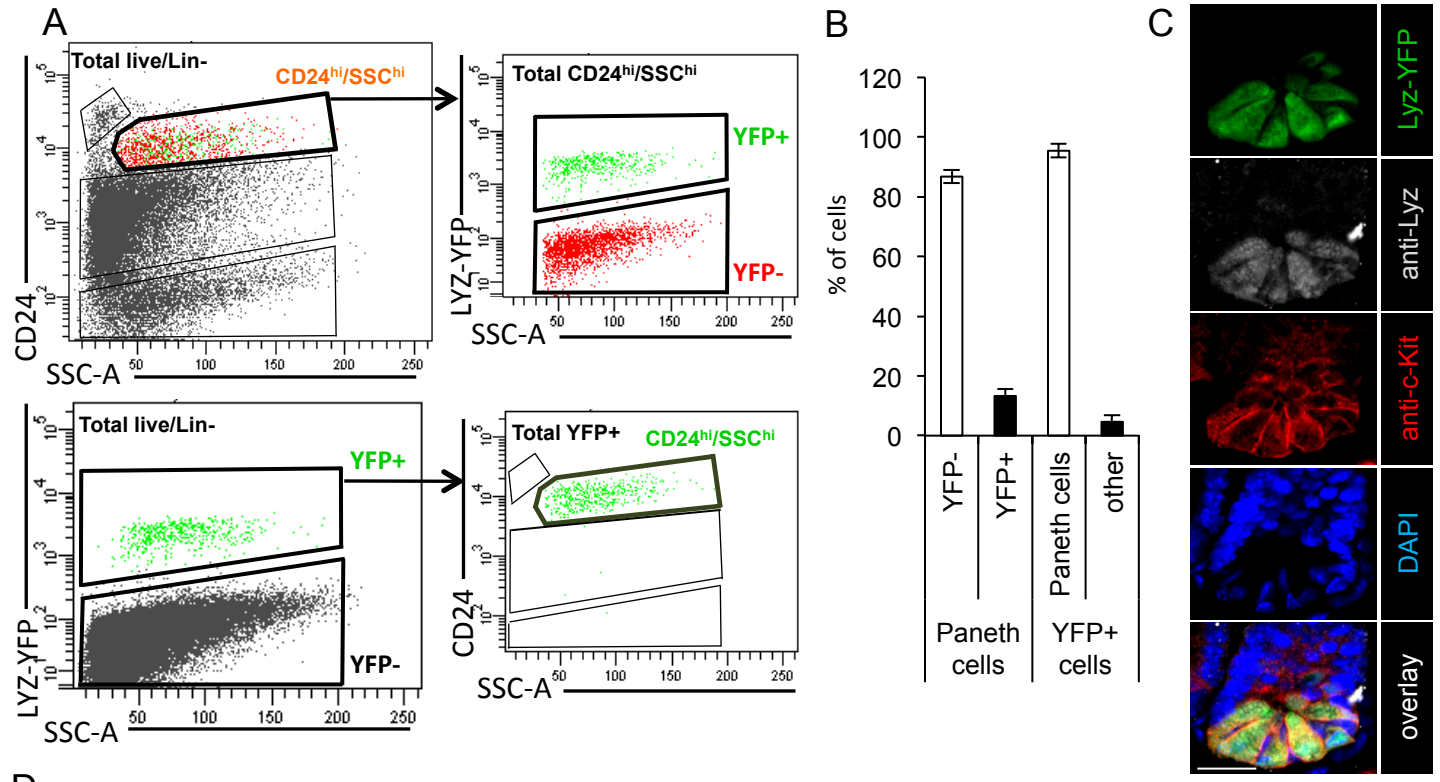

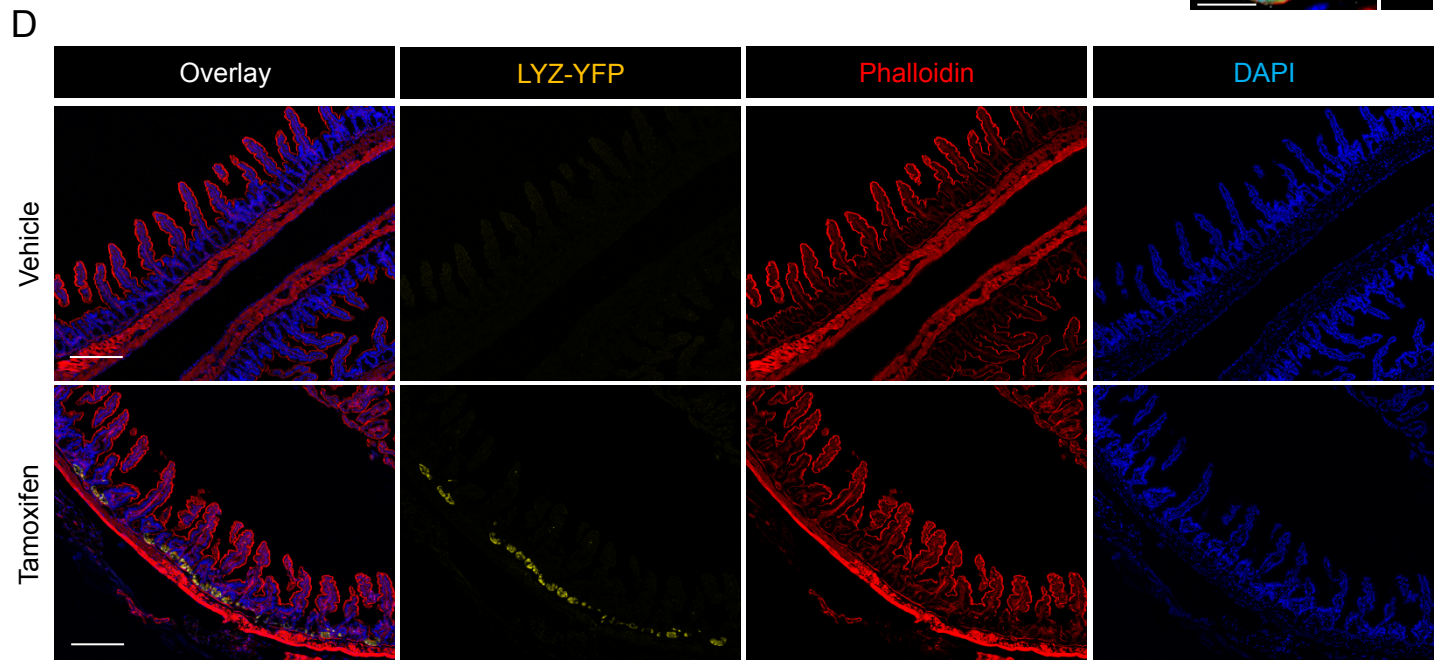

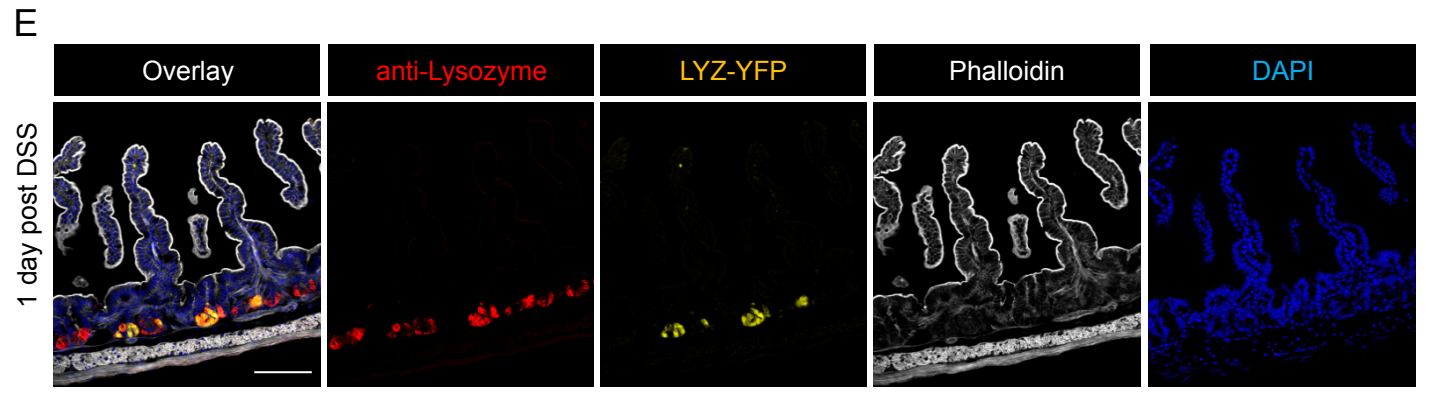

Supplementary Figure 4 (related to Figure 4)

A) FACS analysis of Paneth cells and YFP^+ cells of Tamoxifen injected Lyz-Cre/R26-LSL-YFP mice. Upper left plot: selection of Paneth cells using a standard $CD24^{high}/SSC^{high}$ gate on total live/Lin- cells. Red labelled cells within the highlighted $CD24^{high}/SSC^{high}$ gate are YFP^- Paneth cells, green cells are YFP^+ cells. Upper right plot: $CD24^{high}/SSC^{high}$ cells are subdivided in YFP^+ and YFP^-. Lower left plot: Total live/Lin- cells were subdivided in YFP^+ and YFP^-. Lower right plot: YFP+ cells were analyzed for their distribution in the ($CD24^{high}/SSC^{high}$) Paneth cell region.

B) Quantification of FACS analysis described in B. Approximately 12% of Paneth cells show expression of YFP. 97% of YFP^+ cells were detected within the Paneth cell gate (n=5).

C) Confocal microscopy analysis of Tamoxifen injected Lyz-Cre/R26-LSL-YFP mice using antibodies against lysozyme and c-Kit. YFP labelled cells express lysozyme and c-Kit (scale bar = 25 µm).

D) Analysis of YFP expression in Lyz-Cre/R26-LSL-YFP mice injected with 10% ethanol in sunflower oil (control, upper panel) or Tamoxifen (lower panel) (scale bar = 200µm).

E) Confocal microscopy analysis of Tamoxifen injected Lyz-Cre/R26-LSL-YFP mice using antibodies against lysozyme. The mice were treated for 7 days with 3% DSS and analyzed at day 1 after withdrawal of DSS. Paneth cells are only detected at the base of the crypt and YFP expression could be detected only in $lysozyme^+$ Paneth cells (scale bar = 100µm).

Supplementary Fig. 5 (related to Fig. 5)

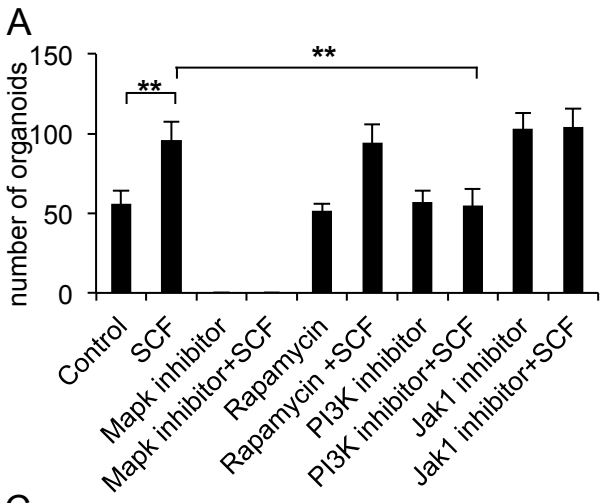

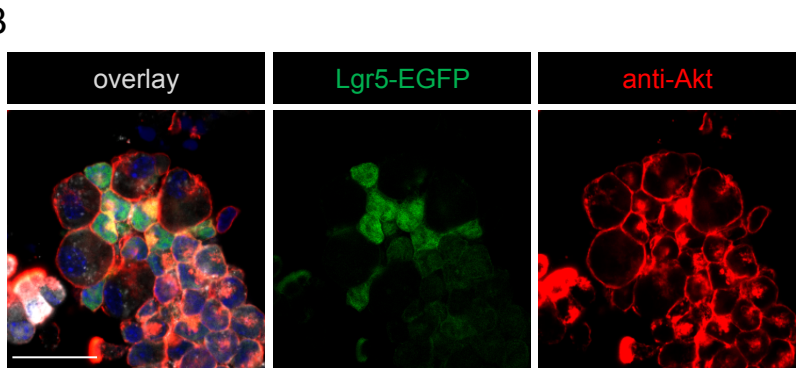

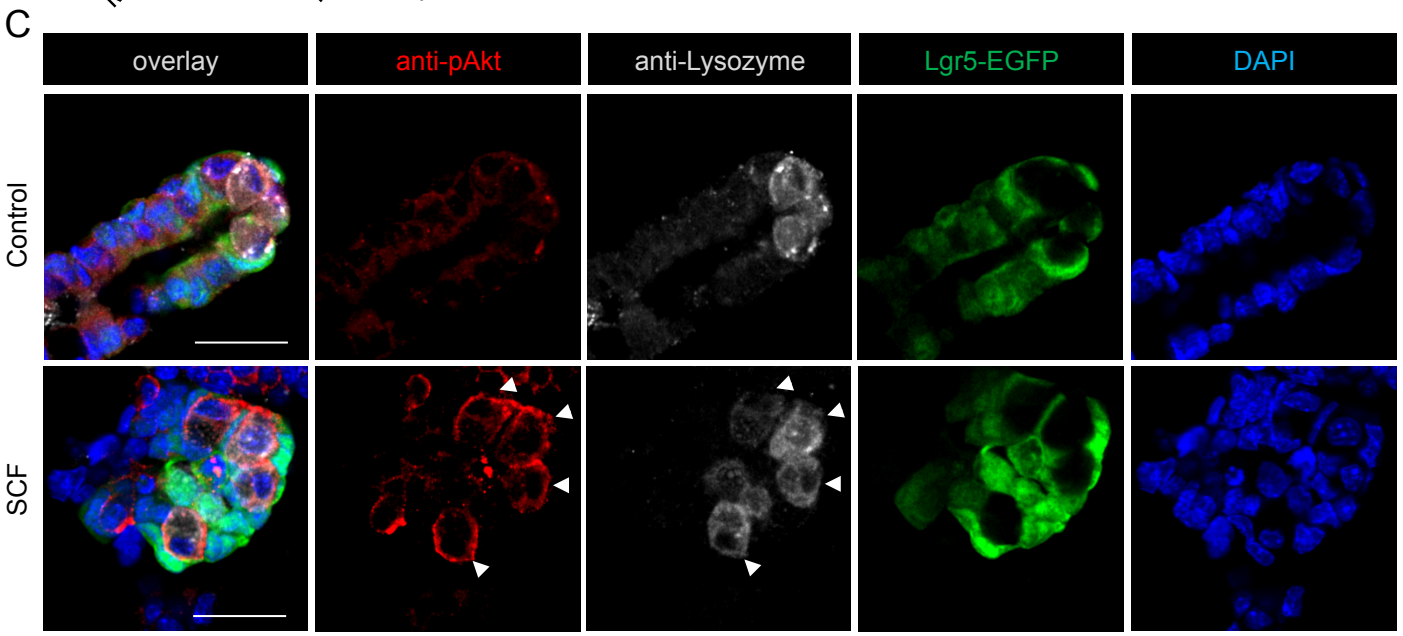

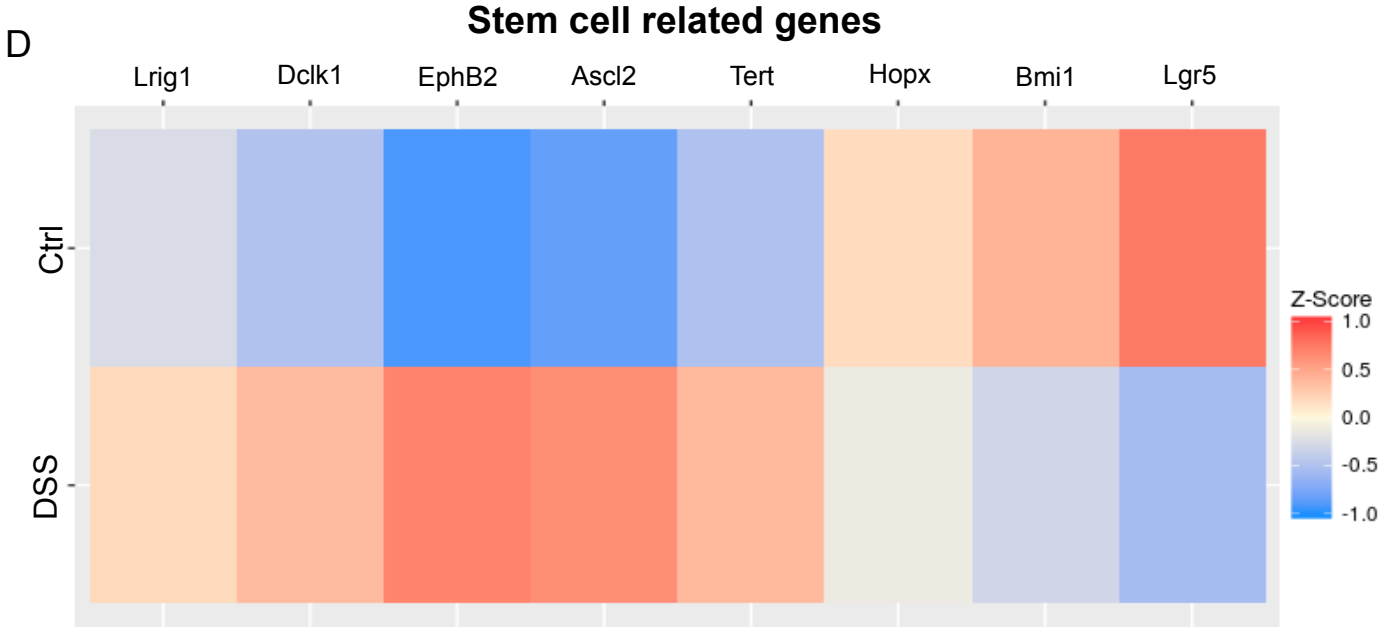

Supplementary Figure 5 (related to Figure 5)

A) Number of organoids derived from untreated or SCF treated (150 ng/ml) whole intestinal crypts. Crypts were plated in the presence or absence of inhibitors against Mapk (U-0126, 1 µM), mTor (Rapamycin 10 nM), PI3K (LY294002, 0.5 µM) or Jak1 (Ruxolitinib, 0.5µM) (**p< 0.01, n=3).

B) Immunostainings for total-Akt in intestinal crypts of *Lgr5*-EGFP mice (scale bar = 25µm). Picture shows one representative example of at least 3 independent experiments.

C) Immunostainings for phospho-Akt and lysozyme in untreated or SCF treated intestinal crypts of *Lgr5*-EGFP mice (arrows indicate phospho-Akt/lysozyme double positive cells, scale bar = 25µm). Picture shows one representative example of at least 3 independent experiments.

D) RNA sequencing analysis of Paneth cells of control or DSS treated mice 3 days after withdrawal of DSS. Heatmap shows differentially expression of stem cell related genes.

Supplementary Fig. 6 (related to Fig. 6)

B

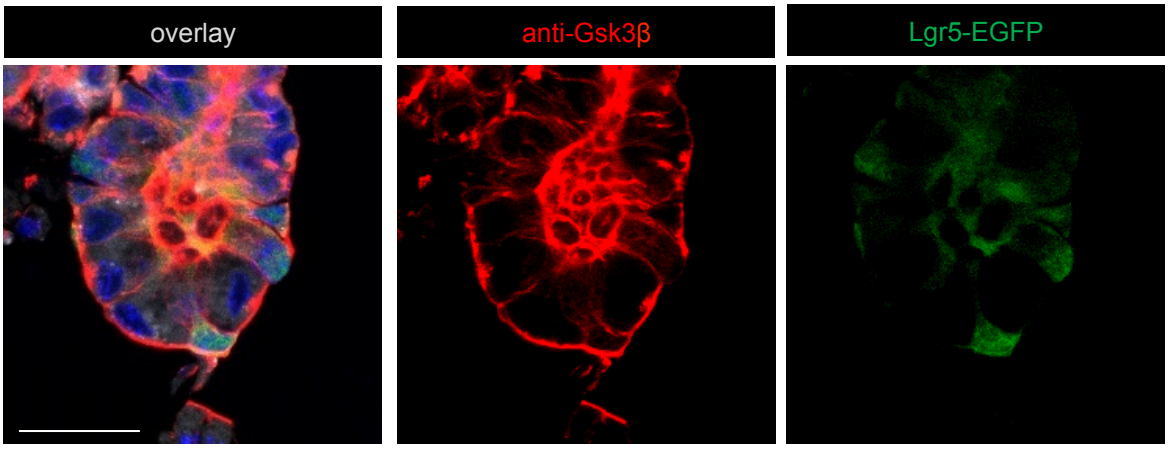

Supplementary Figure 6 (related to Figure 6)

A) Immunostainings for total-GSK3β in intestinal crypts of *Lgr5*-EGFP mice (scale bar = 25µm). Picture shows one representative example of at least 3 independent experiments.

Supplementary Fig. 7 (related to Fig. 7)

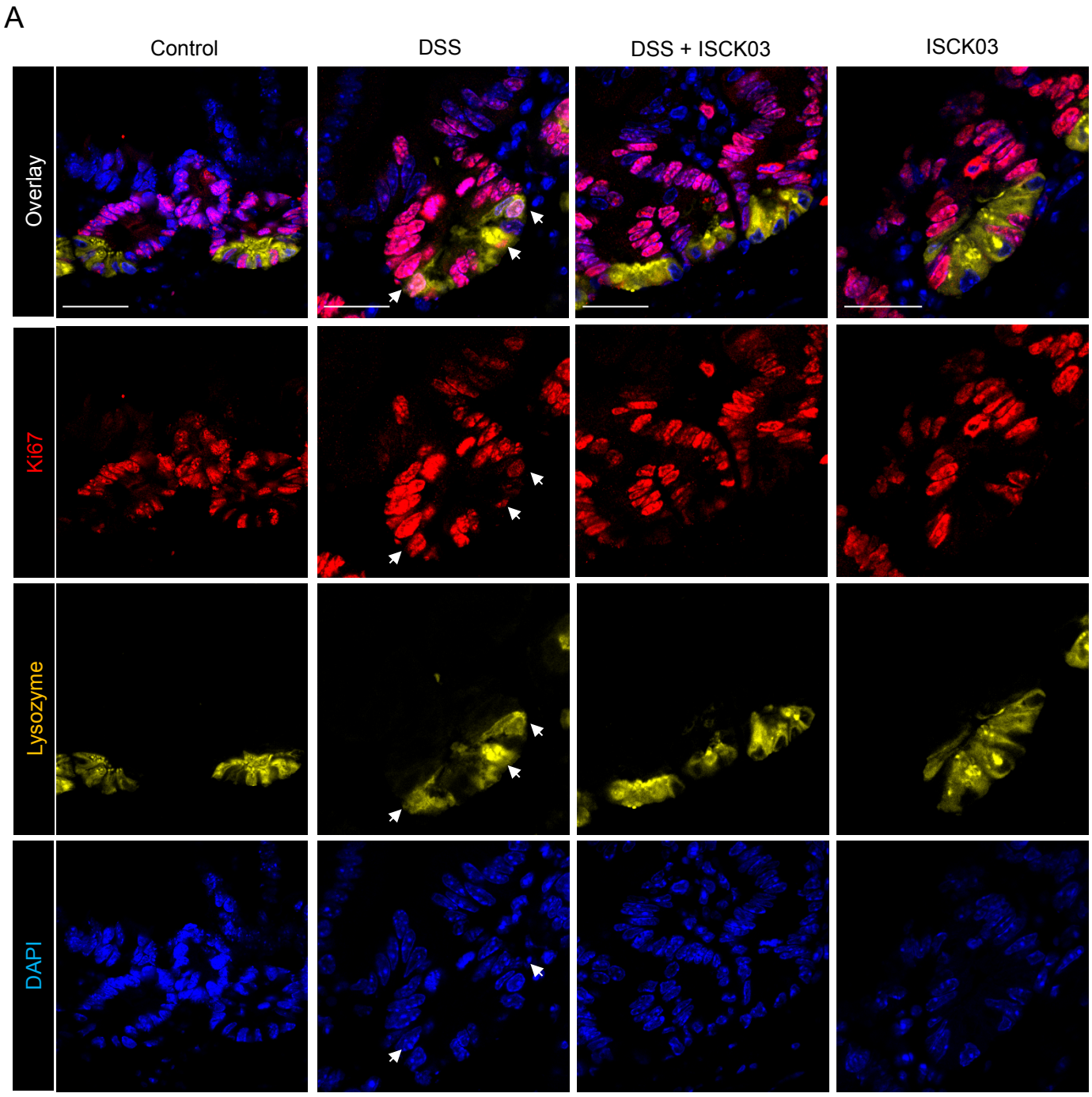

Supplementary Figure 7 (related to Figure 7)

A) Ki67/lysozyme double immunostaining of small intestinal tissues of untreated (left panel), DSS treated (middle left panel), DSS + ISCK03 treated (middle right panel) or ISCK03 treated mice (right panel) or ISCK03 treated mice (right panel). Tissues were harvested 1 day after DSS treatment (arrows indicates a Ki67/lysozyme double positive cell; scale bar = 25 μm).